ARTICLE

Spliced isoforms of the cardiac Nav1.5 channel modify channel activation by distinct structural mechanisms

Adamo S. Mancino[1,2]* , William G. Glass[3]* , Yuhao Yan[1,2], Philip C. Biggin[3] , and Derek Bowie[2]

Alternative splicing is an important cellular mechanism that fine tunes the gating properties of both voltage- and ligand-gated ion-channels. The cardiac voltage-gated sodium channel, Nav1.5, is subject to alternative splicing of the DI S3–S4 linker, which generates two types of channels with different activation properties. Here, we show that the gating differences between the adult (mH1) and neonatal (Nav1.5e) isoforms of Nav1.5 are mediated by two amino acid residues: Thr/Ser at position 207 and Asp/Lys at position 211. Electrophysiological experiments, in conjunction with molecular dynamics simulations, revealed that each residue contributes equally to the overall gating shifts in activation, but that the underlying structural mechanisms are different. Asp/Lys at position 211 acts through electrostatic interactions, whereas Thr/Ser at position 207 is predicted to alter the hydrogen bond network at the top of the S3 helix. These distinct structural mechanisms work together to modify movement of the voltage-sensitive S4 helix to bring about channel activation. Interestingly, mutation of the homologous Asp and Thr residues of the skeletal muscle isoform, Nav1.4, to Lys and Ser, respectively, confers a similar gating shift in channel activation, suggesting that these residues may fulfill a conserved role across other Nav channel family members.

Introduction

Voltage-gated sodium (Nav) channels make up a family of ion channels that are essential to excitable tissues for their contribution to the upstroke of the action potential (Catterall, 2012; Ahern et al., 2016). Nav channels are 260 kD (~2,000-amino-acid-long) monomeric proteins that can be divided into four homologous domains, DI through DIV (Talvenheimo et al., 1982; Noda et al., 1984). Each domain consists of six transmembrane helices (S1–S6), which can be further divided into two components, with S1–S4 forming the voltage-sensor domain (VSD) and S5–S6 making up the pore domain (Catterall, 2010; Payandeh et al., 2011; Jiang et al., 2020). In mammals, there are nine different Nav channel isoforms, Nav1.1 through to Nav1.9, all of which are encoded by distinct genes, SCNXA where X = [1–5, 8–11] (Goldin et al., 2000). This large diversity allows Nav channels to fulfill their widespread roles across many tissues, including in the heart, the nervous system and skeletal muscle (Ahern et al., 2016). Nav channel isoforms can be further categorized according to their phylogeny and functional behavior. Nav1.5, Nav1.8, and Nav1.9 form one subfamily, due to their high sequence similarity and shared resistance to the pufferfish toxin, tetrodotoxin (TTX). Another closely related cluster of

TTX-sensitive channels is comprised of Nav1.1, Nav1.2, Nav1.3, and Nav1.7. The remaining two channels, which are also TTX-sensitive, Nav1.4 and Nav1.6, bridge the gap between the other two groups (Goldin et al., 2000; Goldin, 2002).

Further diversity in the Nav channel family is achieved through alternative splicing. Although each isoform has a unique profile of alternative splicing, there is one feature that is conserved across most isoforms. In six of the Nav channel genes, there exist two forms of the gene sequence encoding the top of the S3 helix through to the bottom of the S4 helix of the DI VSD, named the neonatal and the adult cassettes according to their developmental expression patterns (Copley, 2004; Gazina et al., 2010; Schroeter et al., 2010). S3–S4 splicing in DI has one of two major functional consequences on channel gating. In Nav1.1, Nav1.2, and Nav1.7, splicing of the DI S3–S4 linker affects channel inactivation (Chatelier et al., 2008; Fletcher et al., 2011; Liavas et al., 2017). Similar splicing in Nav1.5, in contrast, has been shown to shift the voltage-dependence of channel activation (Onkal et al., 2008). Despite this, the exact molecular mechanism by which alternate splicing of the DI S3–S4 linker impacts the VSD has not been fully explored. It has been

[1]Integrated Program in Neuroscience, McGill University, Montréal, Quebec, Canada; [2]Department of Pharmacology and Therapeutics, McGill University, Montréal, Quebec, Canada; [3]Department of Biochemistry, University of Oxford, Oxford, UK.

*A.S. Mancino and W.G. Glass contributed equally to this paper. Correspondence to Derek Bowie: derek.bowie@mcgill.ca.

proposed that the aspartate-lysine amino acid switch in Nav1.5 accounts for the entire effect on channel activation (Onkal et al., 2008). Exactly how the Asp/Lys position exerts its effect and whether other residues within the S3–S4 linker contribute to shifting channel activation has not been investigated. It is also unclear why splicing in the S3–S4 linker of other Nav channel isoforms yields significantly different effects on channel function.

To understand these questions, we first focused our attention on Nav1.5 channels to study how alternate splicing of the DI S3–S4 linker affects channel function. Contrary to previous studies, we show that shifts in channel activation due to alternate splicing are due to two (not just one) amino acid residues, namely Thr/Ser at position 207 and Asp/Lys at position 211. Furthermore, we establish that removal of the negative charge at position 211 and loss of the hydrogen bond donor at position 207 are sufficient to promote a depolarization shift in the voltage dependence of Nav1.5. This experimental finding is supported by molecular dynamics simulations, which suggest that the T207S and D211K mutations alter VSD interactions to ultimately hinder S4 translocation and, by extension, channel gating. Finally, we were able to confer an identical gating shift in Nav1.4 channels by mutating these residues, even though the S3–S4 linker of this isoform is not subject to alternative splicing (Loussouarn et al., 2015). This latter finding demonstrates that the impact on channel activation over inactivation is not unique to Nav1.5, suggesting the existence of a conserved DI architecture within the Nav channel family.

Materials and methods

Site-directed mutagenesis
The mouse Nav1.5 (mNav1.5) gene in a pcDNA3 vector was obtained from Dr. T. Zimmer (Friedrich Schiller University, Jena, Germany; Camacho et al., 2006). Exon 6a cDNA was amplified out of mouse brain homogenate, using the access RT-PCR System (Promega), and then exchanged with exon 6b in mNav1.5 using the Quikchange method of site-directed mutagenesis (Braman et al., 1996), to yield the mNav1.5e transcript. The mouse $\beta3$ plasmid was similarly cloned into a pcDNA3 vector from mouse brain homogenates. The mouse Nav1.4 (mNav1.4) gene in a pCMV6-Entry plasmid was purchased from Origene and modified to remove added tags and to introduce a GFP-like fluorophore (Mystik) conjugated upstream to the Nav gene by means of a P2A vector.

All subsequent point mutations of the mNav1.5, mNav1.5e, and mNav1.4 templates were carried out via the single-primer reaction in parallel (SPRINP) variant of PCR (Edelheit et al., 2009). Briefly, 30–60-nucleotide-long primers (Integrated DNA Technologies) were designed, containing both the amino acid exchange of interest and an appropriate silent restriction site. After PCR, unmutated templates were digested using DpnI restriction endonuclease (New England Biolabs) at 37°C for ≥3 h. Part of the PCR mixture was then transformed into 100 µl of house-grown DH5α-competent *Escherichia coli*. Transformed bacteria were grown on agar plates overnight, and single colonies were subsequently cultured in 25 g/liter lysogeny broth

(Fisher Bioreagents). Plasmids were extracted using either QIAprep Spin Miniprep Kits (Qiagen) or, in case of amplification, QIAfilter Plasmid Maxi Kits (Qiagen). Mutations were screened via restriction digestion and gel electrophoresis, using silent restriction sites initially designed into the site-directed mutagenesis primers. Final confirmation that the intended mutation was incorporated without off-target mutations came from Sanger sequencing by the Innovation Centre of McGill University and Genome Quebec. Analyses of sequences were done using Sequencher v4.8 and CLC Sequence Viewer v8.0 programs.

Cell culturing and transfection protocols
Variants of human embryonic kidney cells overexpressing the SV40 large T-antigen (i.e., HEK-293T) were used as the expression vehicle for electrophysiology recordings. Cell cultures were maintained in minimal essential medium containing Glutamax (MEM-glutamax; Gibco) supplemented with 10% FBS (Gibco) and incubated in a ThermoForma Series II Water-Jacketed CO_2 Incubator (Thermo Fisher Scientific) at 37°C, 100% humidity, and 5% CO_2.

Cells in 35-mm tissue culture–treated culture dishes (Corning) were transiently transfected ≥24 h before recording, using the calcium phosphate transfection method (Jordan et al., 1996). 0.5 µg of the intended Nav channel plasmid, 0.2 µg of Mystik, as a transfection reporter, and where needed, 0.75 µg of $\beta3$ were mixed together with 560 mM of $CaCl_2$ (unless otherwise indicated, all chemical reagents were from Sigma-Aldrich). Precipitates could form over 30–60 s after addition of an equal volume of 2XBES solution (in mM: 50 BES, 280 NaCl, and 1.5 Na_2HPO_4) before being added to a single culture dish. The transfection was quenched 6–9 h later by rinsing with PBS (in mM: 137 NaCl, 2.7 KCl, 10.1 Na_2HPO_4, and 2 NaH_2PO_4) supplemented with 1 mM EDTA, PBS supplemented with 1 mM $MgCl_2$ and 1 mM $CaCl_2$, and finally, fresh culture medium. Transfected HEK-293T cells were incubated overnight to recover.

Electrophysiology
At least 2 h before an experiment, transfected cells were dissociated using Accutase and replated at a lower density onto culture dishes. This step increased the yield of isolated cells, overcoming the voltage-clamp issues that arise from the gap junctions that form spontaneously between neighboring HEK-293T cells (Qiao and Sanes, 2015).

Recordings of transiently transfected Nav currents were made using the whole-cell patch clamp configuration (Sakmann and Neher, 1984). Cells were bathed in external solution containing (in mM): 155 NaCl, 4 KCl, 5 HEPES, 1 $MgCl_2$, and 1.8 $CaCl_2$, with pH adjusted to 7.3–7.4 using NaOH. Cells were patched with microelectrodes containing the following internal solution (in mM): 115 CsCl, 5 HEPES, 5 Cs_4-BAPTA, 1 $MgCl_2$, 0.5 $CaCl_2$, and 10 Na_2ATP, with pH adjusted to 7.3–7.4 with CsOH and osmolality of 295–305 mOsm to match the osmolality of the external solution, adjusted by addition of sucrose. Borosilicate glass capillaries (inner diameter 1.15 mm, outer diameter 1.65 mm, length 100 mm, and 0.1-mm filament; King Precision Glass) were pulled using a PP-830 vertical puller (Narishige), yielding

Mancino et al.
Splice variants of Nav1.5 alter activation by distinct mechanisms

Journal of General Physiology   2 of 17
https://doi.org/10.1085/jgp.202112906

microelectrodes with a pipette resistance of 1–5 MΩ. Microelectrode tips were then dipped into Bees-Wax Pure Natural (Integra Miltex) and subsequently fire-polished with an MF-900 Micro Forge (Narishige) to reduce noise and improve membrane seals. Dissociated cells were visualized using an Eclipse Ti-U Inverted Microscope (Nikon), and transfected cells were identified by their green fluorescence, excited by a DC4104 4-Channel LED Driver (Thorlabs). Electrodes were filled with positive pressure orally and lowered to the cell surface by means of an MP-285 micromanipulator (Sutter Instrument). Release of the positive pressure led to >1 GΩ seal, and negative pressure was applied to break the seal and enter the whole-cell configuration. Voltage commands were delivered through an AxoPatch 200B Amplifier (Axon Instruments). Capacitive transients from the pipette and from the cell were cancelled, cell capacitance and series resistance were monitored to avoid changes exceeding 30%, and series resistance was compensated to the amplifier's maximum (98% on the machine, in practice probably closer to 80%). Currents were acquired at 100 kHz, low-pass Bessel filtered at 5 kHz using a Model 900 Tunable Active Filter (Frequency Devices), and telegraphed via an Axon Digidata 1550 (Molecular Devices). All data was collected and saved digitally using pClamp 10.7 software (Axon Instruments).

Voltage-clamp protocols

Cells were clamped at a holding potential of –60 mV between protocols and between sweeps within a protocol. Leak subtraction was instead performed in a custom Igor Pro (WaveMetrics) program post hoc. Three default protocols were applied to study recombinant Nav1.5.

(1) Activation protocol: cells were stepped down to –100 mV for 300 ms, depolarized to a series of potentials between –110 and +70 mV in increments of 5 mV for 100 ms, and returned to –100 mV for another 300 ms. (2) Steady-state inactivation protocol: Cells were stepped down to –100 mV for 300 ms, given a prepulse that varied between –160 mV and –30 mV in increments of 5 mV for 100 ms, given a test pulse to –10 mV to elicit a current for 50 ms, and returned to –100 mV for an additional 300 ms. (3) Recovery from inactivation protocol: This was achieved using two separate protocols. Cells were stepped down to –100 mV for 300 ms, given a first test depolarizing step to –10 mV for 80 ms, returned to –100 mV for a variable amount of time, provided a second depolarizing step to –10 mV for 80 ms, and returned to –100 mV for 300 ms. In the first protocol, the interpulse interval varied from 1 to 25 ms in increments of 1 ms, whereas in the second protocol, the interpulse interval varied from 10 to 150 ms in increments of 10 ms.

There was one deviation from these protocols. mNav1.4 channels would activate only at potentials substantially more positive than Nav1.5. Therefore, test pulses were adjusted to +10 mV as opposed to –10 mV, to improve current resolution during protocols of inactivation and recovery from inactivation.

Electrophysiology data analysis

Analysis of electrophysiological recordings was mostly done using a custom automated script in Igor Pro. Each of the voltage-clamp protocols described previously were analyzed as follows.

Activation protocol

Sodium conductance at each membrane potential was calculated using Ohm's law:

$$G = \frac{I}{V - E_{Na}},$$

where G is conductance, I is peak current, V is holding potential, and E_{Na} is the reversal potential for sodium. E_{Na} was determined by fitting the linear part of the current–voltage curve to a line and extrapolating to the x-intercept. Conductance was then plotted as a function of voltage and fitted according to the Boltzmann function:

$$G = \frac{G_{max}}{1 + e^{-\frac{V - V_{1/2}}{k}}},$$

where G is conductance, V is voltage, G_{max} is the maximum conductance, $V_{1/2}$ is the half-activation potential, and k is the slope factor of voltage sensitivity. A normalized conductance–voltage fit could then be obtained by dividing all conductance values by G_{max} and fitting these normalized conductance values again to the Boltzmann function, this time fixing $G_{max} = 1$. The $V_{1/2}$ and k values for all conditions are tabulated in Table 1.

Activation $V_{1/2}$ values for a given condition were found to span a large ~15-mV range, much larger than the shifts that we attempted to resolve. To control this large variability, a moderate correlation was identified between activation $V_{1/2}$ and peak current amplitude in all conditions where peak amplitude ranged beyond 10 nA, such that larger amplitude currents tended to be associated with more hyperpolarized activation $V_{1/2}$ values. To ensure that the reported shifts were real and not an artifact of skewed amplitude distributions (Montnach et al., 2021), scatter plots in which $V_{1/2}$ values were plotted as a function of their corresponding peak current amplitude were reported. The resulting scatter distribution was then fitted with a line of regression:

$$V_x = m * A + b,$$

where V_x is the predicted $V_{1/2}$, m is the line slope, A is the maximum current amplitude, and b is the line y-intercept. The slope and y-intercept for all conditions are tabulated in Table 1.

Steady-state inactivation protocol

Currents were plotted as a function of the prepulse potential and fitted to the following variant of the Boltzmann function:

$$I = \frac{I_{max}}{1 + e^{\frac{V - V_{1/2}}{k}}},$$

where I is current, V is voltage, I_{max} is the maximum current, $V_{1/2}$ is the half-inactivation potential, and k is the slope factor of voltage sensitivity. A normalized current–voltage plot could then be obtained by dividing all currents by I_{max} and fitting again to the modified Boltzmann equation, this time fixing $I_{max} = 1$. The $V_{1/2}$ and k values for all conditions are tabulated in Table 2.

Recovery from inactivation protocol

For every sweep, the current amplitude of the second pulse (I_2) was divided by the current amplitude of the first pulse (I_1), to yield the current fraction recovered (I_2/I_1). Current fractions

Mancino et al.
Splice variants of Nav1.5 alter activation by distinct mechanisms

Journal of General Physiology   3 of 17
https://doi.org/10.1085/jgp.202112906

Table 1. **Activation properties of wild type and mutant Nav1.4 and Nav1.5 sodium channels**

	Activation			Activation $V_{1/2}$ versus peak amplitude		
	$V_{1/2}$ (mV)	k	n	Y-intercept (mV)	Slope (mV/nA)	R coefficient
Splice variants						
mNav1.5	−25.9 ± 0.55	8.2 ± 0.16	36	−22.4 ± 0.13	0.44 ± 0.01	0.45
mNav1.5e	−16.8 ± 0.45	9.0 ± 0.13	51	−14.2 ± 0.08	0.48 ± 0.01	0.40
mNav1.5 + β3	−23.9 ± 1.05	7.9 ± 0.26	11	−20.9 ± 0.79	0.25 ± 0.06	0.15
mNav1.5e + β3	−13.8 ± 0.76	8.9 ± 0.17	18	−10.8 ± 0.21	0.49 ± 0.03	0.52
Single swaps						
mNav1.5-T206V	−25.9 ± 0.57	7.8 ± 0.18	25	−21.2 ± 0.13	0.42 ± 0.01	0.73
mNav1.5e-V206T	−13.0 ± 0.47	9.6 ± 0.10	24	−10.5 ± 0.18	0.55 ± 0.04	0.30
mNav1.5-T207S	−18.2 ± 0.64	9.3 ± 0.15	17	−15.2 ± 0.21	0.68 ± 0.04	0.52
mNav1.5e-S207T	−20.3 ± 0.53	9.6 ± 0.14	26	−17.7 ± 0.13	0.40 ± 0.02	0.51
mNav1.5-T207A	−22.1 ± 0.56	8.3 ± 0.13	26	−18.9 ± 0.16	0.42 ± 0.02	0.48
mNav1.5e-S207A	−16.8 ± 0.49	9.5 ± 0.11	20	−14.5 ± 0.14	0.37 ± 0.02	0.53
mNav1.5-F209N	−25.2 ± 0.57	8.8 ± 0.13	18	−23.0 ± 0.23	0.40 ± 0.04	0.30
mNav1.5e-N209F	−15.5 ± 0.68	8.6 ± 0.14	21	−10.7 ± 0.15	0.60 ± 0.02	0.76
mNav1.5-V210I	−25.2 ± 1.01	8.1 ± 0.27	12	−20.6 ± 0.44	0.46 ± 0.04	0.53
mNav1.5e-I210V	−17.5 ± 0.64	9.2 ± 0.16	24	−13.6 ± 0.14	0.62 ± 0.02	0.68
mNav1.5-D211K	−20.1 ± 0.58	8.6 ± 0.10	24	−17.0 ± 0.19	0.52 ± 0.03	0.40
mNav1.5e-K211D	−23.2 ± 0.50	8.5 ± 0.14	30	−18.5 ± 0.15	0.48 ± 0.01	0.58
mNav1.5-D211A	−21.4 ± 0.75	8.8 ± 0.19	14	−17.9 ± 0.07	0.46 ± 0.01	0.60
mNav1.5e-K211A	−19.8 ± 0.50	8.5 ± 0.18	42	−15.7 ± 0.07	0.47 ± 0.01	0.56
mNav1.5-V215L	−27.0 ± 0.52	8.4 ± 0.16	24	−24.2 ± 0.12	0.44 ± 0.02	0.61
mNav1.5e-L215V	−12.7 ± 0.51	10.1 ± 0.12	21	−10.1 ± 0.18	0.55 ± 0.03	0.41
mNav1.5-S234P	−24.2 ± 0.71	8.1 ± 0.23	20	−19.9 ± 0.16	0.56 ± 0.02	0.73
mNav1.5e-P234S	−14.7 ± 0.48	9.9 ± 0.13	18	−12.4 ± 0.19	0.61 ± 0.04	0.39
Double swaps						
mNav1.5-T207S-D211K	−16.2 ± 0.50	9.3 ± 0.10	25	−13.3 ± 0.16	0.50 ± 0.02	0.43
mNav1.5e-S207T-K211D	−27.6 ± 0.51	8.8 ± 0.16	24	−23.9 ± 0.17	0.46 ± 0.02	0.51
SCN4A						
Mys-P2A-mNav1.4 + β3	−2.3 ± 0.65	8.8 ± 0.21	13	0.48 ± 0.31	1.4 ± 0.14	0.43
Mys-P2A-mNav1.4-T207S-D211K + β3	5.7 ± 0.50	9.0 ± 0.24	25	5.9 ± 0.18	0.12 ± 0.02	0.0032

recovered were then plotted against their corresponding inter-pulse intervals (t), and fitted with the double exponential

$$\frac{I_2}{I_1} = 1 + A_1 e^{\frac{-t}{\tau_1}} + A_2 e^{\frac{-t}{\tau_2}},$$

where A_1 is the weight of time constant τ_1 and A_2 is the weight of time constant τ_2. The smaller of τ_1 and τ_2 became the fast time constant, and the larger the slow time constant. The weighted τ, τ_{wei}, was then calculated as follows:

$$\tau_{wei} = \frac{A_1\tau_1 + A_2\tau_2}{A_1 + A_2}.$$

The weighted τ values, individual τ (fast and slow) values, and their respective weightings for all conditions are tabulated in Table 2.

Data are presented as mean ± SEM, unless otherwise indicated. Statistical significance of the differences in $V_{1/2}$, k, and τ values was determined by a Student's unpaired t test in the basic two-sample comparisons of mNav1.5e and mNav1.5 as well as mNav1.4 + β3 and mNav1.4-T207S-D211K + β3. In all subsequent cases, we used a one-way ANOVA with Tukey's honestly significant difference post hoc test, always including mNav1.5 and mNav1.5e where appropriate. In the case of scatter plots, statistical significance of the differences in slopes and intercepts was assessed by a regression analysis with Tukey-type multiple regressions. All statistical tests were built into Igor Pro.

Molecular dynamics simulations

All simulations were performed using GROMACS 2020.3 (Abraham et al., 2015) with the following forcefields: AMBER

Mancino et al.
Splice variants of Nav1.5 alter activation by distinct mechanisms

Journal of General Physiology 4 of 17
https://doi.org/10.1085/jgp.202112906

Table 2. **Inactivation properties of wild type and mutant Nav1.4 and Nav1.5 sodium channels**

	Inactivation			Recovery from inactivation						
	$V_{1/2}$ (mV)	k	n	Weighted τ (ms)	Fast (τ [ms])	% (Fast)	Slow (τ [ms])	% (Slow)	n
Splice variants									
mNav1.5	−82.1 ± 0.82	−6.9 ± 0.16	34	12.7 ± 1.06	5.8 ± 0.22	79	38.1 ± 3.49	21	22
mNav1.5e	−82.0 ± 0.52	−7.2 ± 0.14	49	12.4 ± 0.41	6.2 ± 0.19	78	34.6 ± 1.24	22	46
mNav1.5 + β3	−76.3 ± 0.66	−5.7 ± 0.12	12	5.2 ± 0.46	4.0 ± 0.20	83	11.1 ± 4.02	17	12
mNav1.5e + β3	−74.5 ± 0.55	−6.2 ± 0.19	17	4.9 ± 0.24	3.5 ± 0.17	70	8.0 ± 1.24	30	15
Single swaps									
mNav1.5-T206V	−81.3 ± 0.61	−6.9 ± 0.35	21	13.2 ± 0.86	6.4 ± 0.25	78	38.6 ± 3.11	22	22
mNav1.5e-V206T	−81.5 ± 0.49	−7.5 ± 0.18	24	12.7 ± 0.40	6.1 ± 0.18	77	36.3 ± 2.04	23	23
mNav1.5-T207S	−87.3 ± 1.05	−7.4 ± 0.22	14	14.4 ± 1.00	7.3 ± 0.53	74	36.0 ± 2.69	26	11
mNav1.5e-S207T	−83.4 ± 0.48	−7.0 ± 0.09	25	14.0 ± 0.50	7.0 ± 0.28	78	39.9 ± 1.98	22	24
mNav1.5-T207A	−81.9 ± 0.43	−7.0 ± 0.21	25	15.1 ± 0.65	7.3 ± 0.26	78	43.8 ± 2.70	22	23
mNav1.5e-S207A	−80.2 ± 0.62	−7.6 ± 0.20	18	12.1 ± 0.46	5.5 ± 0.19	76	33.9 ± 2.14	24	17
mNav1.5-F209N	−82.4 ± 0.77	−8.0 ± 0.29	18	11.2 ± 0.76	5.5 ± 0.18	78	32.0 ± 3.40	22	18
mNav1.5e-N209F	−79.9 ± 0.40	−6.7 ± 0.09	21	11.3 ± 0.35	5.7 ± 0.16	80	35.9 ± 1.86	20	21
mNav1.5-V210I	−81.1 ± 1.96	−7.6 ± 0.42	11	14.4 ± 1.00	6.7 ± 0.50	79	44.3 ± 3.92	21	11
mNav1.5e-I210V	−82.0 ± 0.45	−6.9 ± 0.13	23	12.3 ± 0.52	5.8 ± 0.19	77	35.1 ± 2.28	23	19
mNav1.5-D211K	−82.8 ± 0.59	−7.3 ± 0.12	24	13.3 ± 0.56	7.2 ± 0.67	80	37.2 ± 1.96	20	21
mNav1.5e-K211D	−80.3 ± 0.54	−6.9 ± 0.12	30	10.4 ± 0.44	5.3 ± 0.23	80	31.5 ± 1.31	20	29
mNav1.5-D211A	−79.8 ± 0.54	−7.2 ± 0.22	15	11.0 ± 0.38	5.3 ± 0.21	78	32.8 ± 1.90	22	15
mNav1.5e-K211A	−80.0 ± 0.48	−6.7 ± 0.08	39	10.2 ± 0.37	5.2 ± 0.20	79	29.7 ± 1.53	21	34
mNav1.5-V215L	−84.6 ± 0.54	−6.4 ± 0.08	24	14.3 ± 0.71	7.3 ± 0.44	78	40.3 ± 2.36	22	21
mNav1.5e-L215V	−82.8 ± 0.76	−7.2 ± 0.11	20	13.9 ± 0.62	7.1 ± 0.36	76	36.9 ± 2.06	24	19
mNav1.5-S234P	−81.3 ± 0.55	−6.8 ± 0.15	20	11.9 ± 0.50	6.1 ± 0.25	79	34.2 ± 1.41	21	19
mNav1.5e-P234S	−82.5 ± 0.65	−7.9 ± 0.31	18	12.1 ± 0.44	5.9 ± 0.22	80	36.7 ± 1.56	20	18
Double swaps									
mNav1.5-T207S-D211K	−82.7 ± 0.91	−7.4 ± 0.30	25	18.7 ± 1.08	9.5 ± 0.41	75	49.2 ± 4.27	25	24
mNav1.5e-S207T-K211D	−80.9 ± 0.51	−6.5 ± 0.09	23	11.0 ± 0.28	5.5 ± 0.12	78	30.2 ± 1.11	22	23
SCN4A									
Mys-P2A-mNav1.4 + β3	−55.8 ± 0.66	−5.3 ± 0.20	13	1.23 ± 0.18	1.1 ± 0.10	92	2.1 ± 0.81	8	12
Mys-P2A-mNav1.4-T207S-D211K + β3	−55.3 ± 0.36	−5.4 ± 0.15	21	1.04 ± 0.07	0.96 ± 0.06	57	1.3 ± 0.22	43	17

ff99SB-ILDN (Best and Hummer, 2009) for protein and ions, SLipids (Jambeck and Lyubartsev, 2012b, 2012a, 2013) for lipids, and TIP3P (Jorgensen et al., 1983) for water.

The cryo-electron microscope structure of human (h) Nav1.5 (PDB accession no. 6LQA; Li et al., 2021), with all residues resolved, was embedded in a 1-palmitoyl-2-oleoyl-glycero-3-phosphocholine (POPC) membrane consisting of 612 POPC molecules using the CHARMM-GUI (Jo et al., 2017). To avoid unphysical interactions between each domain (DI-IV), terminal residues between DI-DII and DII-DIII were capped with ACE and NME residues in PyMol (Schrödinger, 2015).

The resulting model was used to prepare the hNav1.5-D211K, hNav1.5-T207S, and hNav1.5-D211K-T207S systems using the mutagenesis tool in PyMol. Each system was solvated with water and neutralized with sodium and chloride ions at a

concentration of 150 mM. Energy minimization was performed using the steepest decent algorithm with a force tolerance of 500 kJ mol⁻¹ nm⁻¹ and each system converging within 7,000 steps. Equilibration consisted of a short (5-ns) simulation, where position restraints were applied to all Cα atoms with a force constant of 1,000 kJ mol⁻¹ nm⁻², and a longer (15-ns) simulation, where the Cα position restraints were halved from 1,000 kJ mol⁻¹ nm⁻² every 5 ns to relax the structure into the POPC membrane. Because of the lack of domain linker regions between DI-DII and DII-DIII, distances between capping residues between DI-DII and DII-DIII were maintained in the final frame of the short simulation in both the long equilibration step and subsequent production run simulations. All simulations were carried out in the NPT ensemble. The temperature and pressure were set to 310 K and 1 bar with semi-isotropic pressure

Mancino et al.
Splice variants of Nav1.5 alter activation by distinct mechanisms

Journal of General Physiology 5 of 17
https://doi.org/10.1085/jgp.202112906

coupling and isothermal compressibility set to 4×10^{-5} bar^{-1}. Temperature and pressure were controlled using the Berendsen thermostat and barostat (Berendsen et al., 1984) in the short equilibration with coupling constants set to 0.5 and 5.0 ps, respectively. In the longer equilibrations and production runs the Nosé-Hoover thermostat (Nosé, 1984; Hoover, 1985) and Parrinello-Rahman barostat (Parrinello and Rahman, 1981) with coupling constants of 0.8 and 5.0 ps respectively were used. The van der Waals cut-off was set to 12 Å with dispersion correction for energy and pressure. Electrostatic interactions were treated using the smooth particle mesh Ewald methodology (Darden et al., 1993; Essmann et al., 1995) with a real space cutoff and grid spacing of 12 Å and a grid spacing of 1.6 Å used to obtain the reciprocal energy term in k-space with cubic interpolation. Bonds containing hydrogen were constrained using the LINCS algorithm (Hess et al., 1997). The Verlet cut-off scheme was used with a buffering tolerance of 0.005 kJ mol^{-1} ns^{-1} per particle to construct the pair list. A total of three independent simulations were run for 500 ns each, and coordinates were written out every 250 ps.

Analysis was performed using MDAnalysis (Michaud-Agrawal et al., 2011), where the first 100 ns of each simulation was discarded (unless where otherwise stated) and visualizations were performed in PyMol. All setup, analysis, and visualization scripts (along with software version specifications) can be found at http://github.com/bigginlab/nav-alt-splice. Coordinate and trajectory files for all systems (with solvent removed) can be found at https://zenodo.org/record/5517655.

Results

Alternative splicing of exon 6 selectively alters mNav1.5 channel activation

The gating behavior of the two DI S3–S4 splice variants of Nav1.5 was compared in HEK-293T cells transfected with cDNAs encoding either the adult isoform (here denoted as mNav1.5, where exon 6b is included) or the neonatal isoform (called mNav1.5e, where exon 6a is included). In whole-cell patch-clamp recording mode, channel gating was studied using voltage-clamp protocols to examine channel activation, steady-state inactivation, and recovery from inactivation (Fig. 1).

The activation profile of mNav1.5e was ~10 mV more depolarized than that of mNav1.5, whereas steady-state inactivation and recovery from inactivation were the same for both splice variants. A single Boltzmann function fit well the activation data for both mNav1.5 and mNav1.5e, yielding half-activation potentials ($V_{1/2}$) of −25.9 ± 0.55 mV ($n = 36$) and −16.8 ± 0.45 mV ($n = 51$, P < 0.001), with slope factors (k) of 8.2 ± 0.16 and 9.0 ± 0.13 (P < 0.001), respectively (Fig. 1, B and C; and Table 1). In keeping with this, the range of $V_{1/2}$ values estimated for mNav1.5 and mNav1.5e, when plotted with respect to the peak response amplitude, were parallel (0.44 ± 0.01 and 0.48 ± 0.01 mV/nA, respectively; P = 0.75) between the two isoforms and traversed the vertical (i.e., $V_{1/2}$) axis at different points (−22.4 ± 0.13 and −14.2 ± 0.08 mV; P < 0.001; Fig. 1 D and Table 1). This ensures that the shift in activation $V_{1/2}$ occurs independently of any potential amplitude confound (Montnach et al., 2021), as

explained in Materials and methods. Together, these characteristics highlight the difference in the activation relationships for mNav1.5 and mNav1.5e. In contrast, Boltzmann fits of the steady-state inactivation plots estimated similar $V_{1/2}$ values for mNav1.5 and mNav1.5e, which were −82.1 ± 0.82 mV ($n = 34$) and −82.0 ± 0.52 mV ($n = 49$; P = 0.91; Fig. 1, E and F; and Table 2). The slope factors were also statistically indistinguishable (P = 0.15). Likewise, the double exponential functions used to fit the recovery from inactivation of mNav1.5 and mNav1.5e were the same, with weighted τ values of 12.7 ± 1.06 ms ($n = 22$) and 12.4 ± 0.41 ms ($n = 46$, P = 0.75; Fig. 1 G and Table 2).

Differences in the gating of mNav1.5 and mNav1.5e are due to T207S and D211K residues

Although the two splice variants of exon 6 differ at seven amino acid positions (Fig. 1 A), previous work has proposed that the more depolarized activation of mNav1.5e is due the positively-charged Lys residue at position 211 (Onkal et al., 2008). Consistent with this, replacement of Lys211 in the neonatal transcript with the negatively charged Asp found in mNav1.5 was shown to eliminate the difference in channel activation (Onkal et al., 2008). Because the impact, if any, of the other residues was not examined, we systematically tested all the residues that differ between mNav1.5 and mNav1.5e, including position 211, as single point mutations. This was done in both the forward direction (introducing residues from mNav1.5e into mNav1.5) and reverse direction (introducing residues from mNav1.5 into mNav1.5e).

Unexpectedly, mutation of position 211 in both the forward and reverse directions elicited only a partial shift in the activation curve (Fig. 2). The $V_{1/2}$ value estimated for the forward mutant mNav1.5-D211K was −20.1 ± 0.58 mV ($n = 24$), which was statistically different from both mNav1.5e (P < 0.001) and mNav1.5 (P < 0.001; Fig. 2 A). The y-intercept of the associated $V_{1/2}$ versus amplitude scatter plot measured −17.0 ± 0.19 mV, which was also between mNav1.5 (P < 0.001) and mNav1.5e (P < 0.001; Fig. 2 B). In the reverse direction, the $V_{1/2}$ value for mNav1.5e-K211D was −23.2 ± 0.50 mV ($n = 30$), which differed from mNav1.5 (P < 0.01) and mNav1.5e (P < 0.001; Fig. 2 C). The scatter plot y-intercept agreed with this observation, given that at −18.5 ± 0.15 mV it was distinct from both mNav1.5 (P < 0.001) and mNav1.5e (P < 0.001; Fig. 2 D and Table 1).

All other forward and reverse single point mutations of exon 6 yielded activation curves that were nearly identical to wild type mNav1.5 and mNav1.5e, respectively (Fig. 3). The only exception was position 207, where mutation in the forward direction with mNav1.5-T207S elicited a full shift, whereas mutation in the reverse direction with mNav1.5e-S207T produced a partial shift (Fig. 4). A single Boltzmann function fitted to the activation data for mNav1.5-T207S estimated $V_{1/2}$ to be −18.2 ± 0.64 mV ($n = 17$), which was statistically indistinguishable from that of mNav1.5e (P = 0.30) and therefore distinct from mNav1.5 (Fig. 4 A). At −15.2 ± 0.21 mV, the y-intercept of the mNav1.5-T207S scatter reaffirmed its difference from mNav1.5 (P < 0.001), even though it was no longer overlapping with mNav1.5e (P < 0.05; Fig. 4 B). In contrast, the $V_{1/2}$ value estimated for mNav1.5e-S207T was −20.3 ± 0.53 mV ($n = 26$), which was statistically distinguishable from both mNav1.5

Mancino et al.
Splice variants of Nav1.5 alter activation by distinct mechanisms

Journal of General Physiology   6 of 17
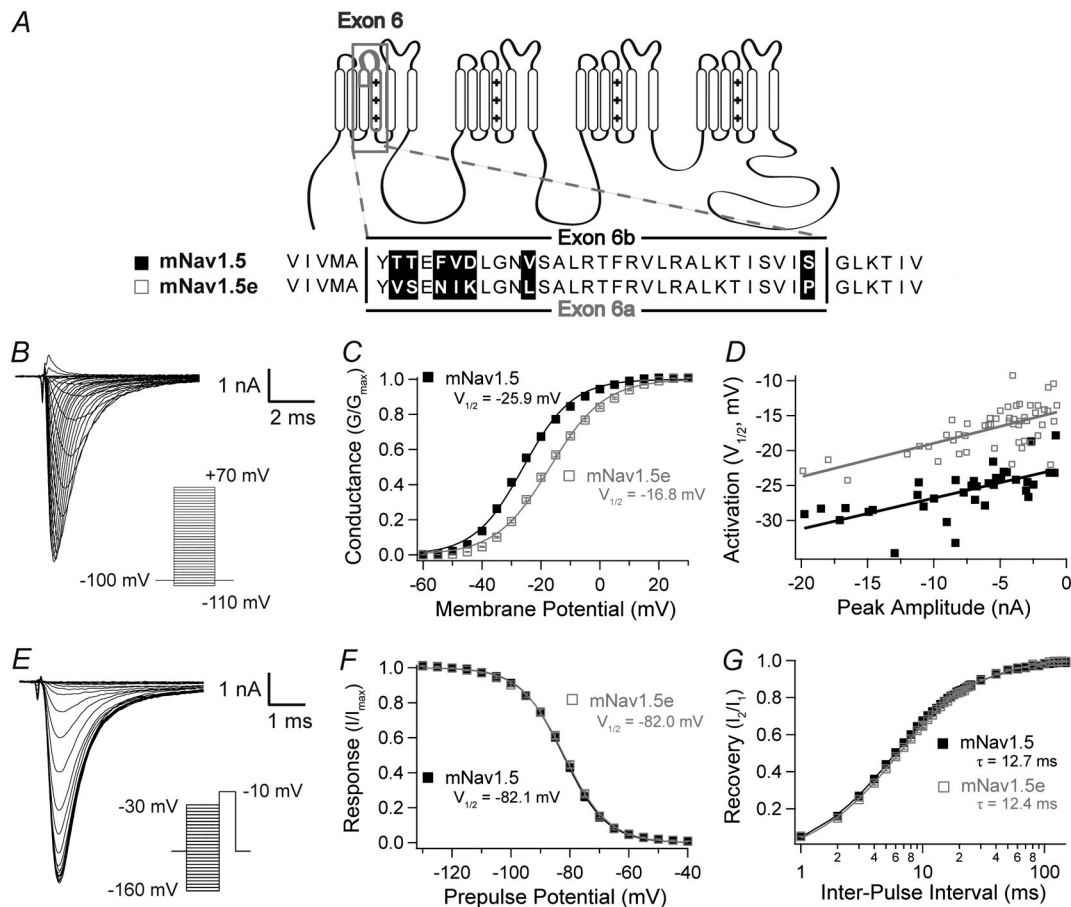https://doi.org/10.1085/jgp.202112906

Figure 1. Alternative splicing at exon 6 selectively alters properties of channel activation. (A) Top: Topology model of Nav1.5. The polypeptide stretch encoded by exon 6, spanning from partway through the S3 segment to the bottom of the S4 segment in DI, is highlighted in the gray box. Bottom: Sequence alignment of exons 6b in mNav1.5 and 6a in mNav1.5e, with the black boxes highlighting the seven amino acid differences between them. **(B)** Sample current traces elicited by Nav1.5 during an activation protocol. Cells were stepped from −100 mV to a range of membrane potentials between −110 mV and +70 mV, in increments of 5 mV. **(C)** Activation profiles of mNav1.5 (black) and mNav1.5e (gray) revealed that mNav1.5e activates at potentials ∼10 mV more depolarized than mNav1.5. $V_{1/2}$ values of mNav1.5e and mNav1.5 were −16.8 ± 0.45 mV (n = 51) and −25.9 ± 0.55 mV (n = 36; P < 0.001), respectively. Slope factor (k) values were 9.0 ± 0.13 and 8.2 ± 0.16, respectively; P < 0.001. **(D)** Distributions of activation $V_{1/2}$ plotted against peak current amplitude reaffirm the 10-mV difference in the activation profiles of mNav1.5 and mNav1.5e. Correlation strength was moderate, with Pearson's r of 0.40 and 0.45 for mNav1.5e and mNav1.5, respectively. Regression line y-intercepts of mNav1.5e and mNav1.5 were −14.2 ± 0.08 and −22.4 ± 0.13 mV (P < 0.001), respectively. Regression line slopes were parallel, at 0.48 ± 0.01 and 0.44 ± 0.01 mV/nA (P = 0.75), respectively, reflecting that the 10-mV difference between mNav1.5e and mNav1.5 was consistent across amplitudes. **(E)** Sample current traces elicited by Nav1.5 during a steady-state inactivation protocol. Cells were given a variable pre-pulse potential, ranging from −160 to −30 mV in increments of 5 mV, then stepped to −10 mV to evoke a current response. **(F)** Inactivation profiles of mNav1.5e and mNav1.5 show that the two splice variants do not differ in terms of steady-state inactivation. $V_{1/2}$ values were −82.0 ± 0.52 mV (n = 49) and −82.1 ± 0.82 mV (n = 34) for mNav1.5e and mNav1.5 (P = 0.91), respectively. k values were −7.2 ± 0.14 and −6.9 ± 0.16 for mNav1.5e and mNav1.5, respectively (P = 0.15). **(G)** mNav1.5e and mNav1.5 do not differ in terms of recovery from inactivation either. The fraction of Nav channels recovered was plotted against the interpulse interval and fitted to a double exponential function, yielding weighted τ values of 12.4 ± 0.41 ms (n = 46) and 12.7 ± 1.06 ms (n = 22) for mNav1.5e and mNav1.5, respectively (P = 0.75).

(P < 0.001) and mNav1.5e (P < 0.001; Fig. 4 C). The associated scatter plot y-intercept was −17.7 ± 0.13 mV, distinct from mNav1.5 (P < 0.001) and mNav1.5e (P < 0.001; Fig. 4 D and Table 1). Therefore, we concluded that position 207 of exon 6 also contributed to the gating difference between mNav1.5 and mNav1.5e.

To examine together the combined role of positions 207 and 211 of exon 6, we tested the gating properties of the forward and reverse double mutations of mNav1.5 and mNav1.5e (Fig. 5). In agreement with our single point mutation data, replacement of Thr207 and Asp211 of mNav1.5 with Ser and Lys of mNav1.5e yielded a profile of activation ($V_{1/2}$, −16.2 ± 0.50 mV, n = 25) that was different from that of mNav1.5 (P < 0.001) and overlapped

with the activation properties of mNav1.5e (P = 0.64; Fig. 5 A). The $V_{1/2}$ versus peak amplitude was consistent with this, with a y-intercept (−13.3 ± 0.16 mV) distinct from mNav1.5 (P < 0.001) and similar to mNav1.5e (P = 0.43; Fig. 5 B). Likewise, the $V_{1/2}$ value for activation of the double mutant, mNav1.5e-S207T-K211D, was −27.6 ± 0.51 mV (n = 25), which was different from mNav1.5e (P < 0.001) but statistically indistinguishable from mNav1.5 (P = 0.10; Fig. 5 C). The associated y-intercept was −23.9 ± 0.17 mV, distinct from mNav1.5e (P < 0.001), although it curiously does overshoot mNav1.5 in the negative direction (P < 0.05; Fig. 5 D and Table 1). Taken together, these data demonstrate that both positions 207 and 211 are
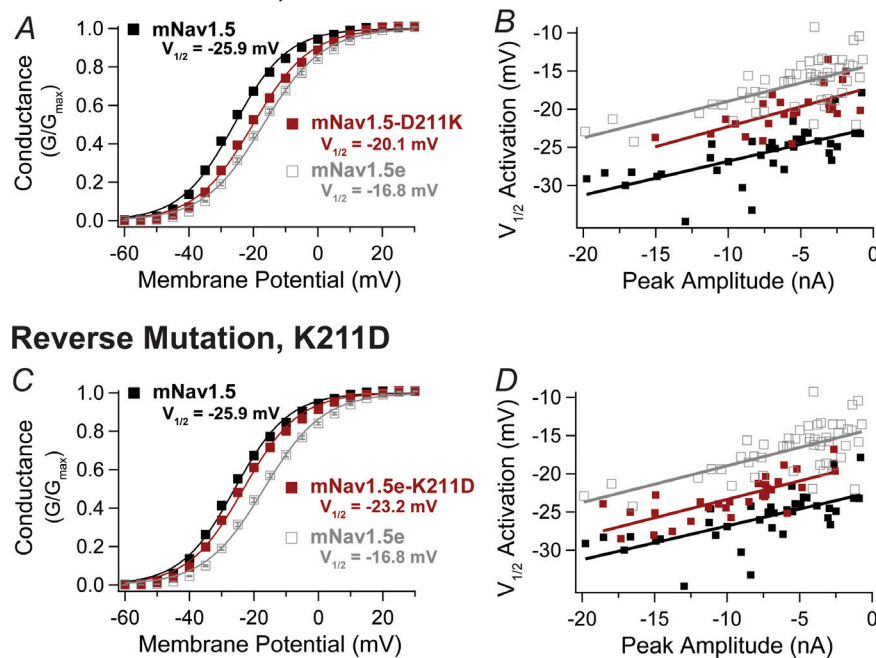
Forward Mutation, D211K

Reverse Mutation, K211D

Figure 2. **The aspartate-lysine switch at position 211 accounts for part of the shift in channel activation. (A)** Introducing D211K into mNav1.5 induces only a partial shift in the activation profile toward that of mNav1.5e. The activation $V_{1/2}$ of mNav1.5-D211K (red) was −20.1 ± 0.58 mV (n = 24), distinct from both mNav1.5 (P < 0.001) and mNav1.5e (P < 0.001). The slope factor k was 8.6 ± 0.10. **(B)** The y-intercept of the mNav1.5-D211K scatter measured −17.0 ± 0.19 mV, different from both mNav1.5 (P < 0.001) and mNav1.5e (P < 0.001). The regression line slope was 0.52 ± 0.03 mV/nA. **(C)** Replacing K211D in mNav1.5e also produces an intermediate phenotype. The activation $V_{1/2}$ of mNav1.5e-K211D (red) was −23.2 ± 0.50 mV (n = 30), distinct from mNav1.5e (P < 0.001) and mNav1.5 (P < 0.01). The slope factor k was 8.5 ± 0.14. **(D)** The y-intercept of the mNav1.5e-K211D scatter measured −18.5 ± 0.15 mV, different from both mNav1.5 (P < 0.001) and mNav1.5e (P < 0.001). The regression line slope was 0.48 ± 0.01 mV/nA.

necessary for the full shift between the two exon 6 splice variants.

The hyperpolarized activation profile of mNav1.5 depends on key chemical moieties

Although we identified the two critical amino acid switches in exon 6, how they affect channel activation remained unclear. We presumed that replacement of Asp with Lys exerted its effect through electrostatic interactions, given the reversal of charge. To test this, we eliminated the charge in both mNav1.5 and mNav1.5e, by introducing alanine at position 211 (Fig. 6). Losing the negative charge in mNav1.5 was no different than gaining the positive charge, given that the activation $V_{1/2}$ of mNav1.5-D211A (−17.9 ± 0.07 mV, n = 14) was indistinguishable from mNav1.5-D211K (P = 0.64; Fig. 6 A). This observation was in agreement with the $V_{1/2}$ versus peak amplitude scatter plot, where the y-intercept of mNav1.5-D211A was −21.4 ± 0.75 mV and thus identical to mNav1.5-D211K (P = 0.92; Fig. 6 B). In contrast, removal of the positive charge from mNav1.5e had a more subtle effect on activation properties. The $V_{1/2}$ value estimated for mNav1.5e-K211A (−19.8 ± 0.50 mV, n = 42) was between mNav1.5e (P < 0.001) and mNav1.5e-K211D (P < 0.001; Fig. 6 C). The scatter plot y-intercept, at −15.7 ± 0.07 mV, differed from both mNav1.5e (P < 0.05) and mNav1.5e-K211D (P < 0.001; Fig. 6 D and Table 1). From this observation, we concluded that the negative charge at position 211 was an important structural feature determining the hyperpolarized activation profile of mNav1.5.

Thr and Ser both have the capacity to form hydrogen bonds yet differ in terms of their flexibility. To determine whether a more constrained or more flexible side chain was important, we made similar mutations of position 207 to alanine (Fig. 7). mNav1.5-T207A had a slightly more depolarized activation

profile compared with wild type, given that its $V_{1/2}$ of −22.1 ± 0.56 mV (n = 26) was different from mNav1.5 (P < 0.001), even though it did not coincide with mNav1.5-T207S (P < 0.001, Fig. 7 A). The same was true of the associated mNav1.5-T207A scatter plot (y-intercept of −18.9 ± 0.16 mV, P < 0.001 compared with mNav1.5, P < 0.01 compared with mNav1.5-T207S; Fig. 7 B). A shift in the activation curve was absent in the reverse mutant. Neither the conductance–voltage plot ($V_{1/2}$ of −16.8 ± 0.49 mV, n = 20) nor the $V_{1/2}$ versus peak amplitude plot (y-intercept of −14.5 ± 0.14 mV) of mNav1.5e-S207A differed significantly from mNav1.5e (P = 1.00 and P = 0.95, respectively; Fig. 7, C and D; and Table 1). We thus concluded that the hyperpolarized activation profile of mNav1.5 required a constrained hydrogen bond donor at position 207.

Molecular dynamics simulations predict that T207S and D211K destabilize DI

To provide a better mechanistic insight into the impact of exon 6, a series of MD simulations were performed on hNav1.5, hNav1.5-T207S, hNav1.5-D211K, and the double hNav1.5-T207S-D211K mutants (Fig. 8). Within the DI VSD, there exists a network of charged residues (Fig. 9). This includes the gating charges which respond to differences in membrane potential, countercharges that stabilize the gating charges, as well as charged phospholipid head groups in the surrounding membrane (Catterall, 2010). To investigate any change that residues at positions 207 and 211 may cause in the VSD, we measured the distances of potential salt bridges. In both hNav1.5-D211K and hNav1.5-T207S-D211K, there was an increased interaction of K211 with the head groups of the phosphatidylcholine membrane (Fig. 8 A). This, in turn, distorted the top of the VSD (Fig. 8 B). The introduction of D211K also caused an increase in the distance between R219/R222 and E208 (Fig. 10 B), while in

Forward Mutations: T206V, F209N, V210I, V215L, S234P

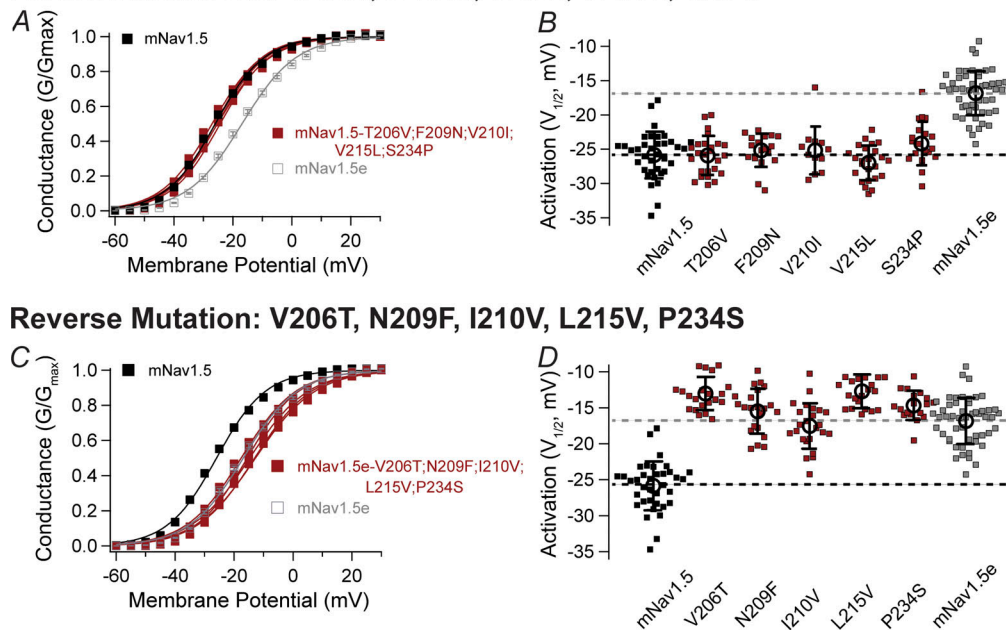## Reverse Mutation: V206T, N209F, I210V, L215V, P234S

Figure 3. Most other amino acid exchanges serve negligible roles in setting channel activation following exon 6 splicing. (A) With the exception of Thr/Ser at position 207, none of the other amino acid exchanges in exon 6 can be introduced into mNav1.5 to render it mNav1.5e-like. The $V_{1/2}$ values of mNav1.5-T206V, mNav1.5-F209N, mNav1.5-V210I, mNav1.5-V215L, and mNav1.5-S234P were −25.9 ± 0.57 mV ($n = 25$), −25.2 ± 0.57 mV ($n = 18$), −25.2 ± 1.01 mV ($n = 12$), −27.0 ± 0.52 mV ($n = 24$), and −24.2 ± 0.52 mV ($n = 20$), respectively. None of these conditions differed significantly from mNav1.5 (P = 0.07). **(B)** Scatter dot plot showing the spread of $V_{1/2}$ values across the different possible amino acid swaps of positions 206, 209, 210, 215, and 234, engineered into mNav1.5. Individual $V_{1/2}$ values are shown as squares. The hollow circle represents the mean. Error bars reflect 1 SD, not SEM. **(C)** Apart from Thr/Ser at position 207, none of the other amino acid exchanges in exon 6 can be introduced into mNav1.5e to render it mNav1.5-like. The $V_{1/2}$ values of mNav1.5e-V206T, mNav1.5e-N209F, mNav1.5e-I210V, mNav1.5e-L215V, and mNav1.5e-P234S were −13.0 ± 0.47 mV ($n = 24$), −15.5 ± 0.68 mV ($n = 21$), −17.5 ± 0.64 mV ($n = 24$), −12.7 ± 0.51 mV ($n = 21$), and −14.7 ± 0.48 mV ($n = 18$), respectively. While some of these conditions differed significantly from mNav1.5e (P < 0.001), those were curiously all shifted to more depolarized potentials than mNav1.5e itself. **(D)** Scatter dot plot showing the spread of $V_{1/2}$ values across the different possible amino acid swaps of positions 206, 209, 210, 215, and 234, engineered into mNav1.5e. Individual $V_{1/2}$ values are shown as squares. The hollow circle represents the mean. Error bars reflect 1 SD, not SEM.

hNav1.5-T207S-D211K the R222–E208 interaction was partially restored (Fig. 10 C). From this, we postulated that these events contribute to increased steric strain and disruption in the S3–S4 linker (Fig. 8 C), potentially hindering S4 translocation upon depolarization.

The exact nature of how the T207S mutation influences the interactions in the VSD was slightly more elusive. In hNav1.5, the presence of the secondary alcohol group in T207 stabilized the side chain of E208 to transiently interact within the DI VSD and in particular with R219, located in the S4 helix. In hNav1.5-T207S, this interaction was seen more frequently, due to the loss of a stabilizing hydrogen bond between the secondary alcohol group of T207S and side chain of E208, instead favoring the backbone oxygen of M203 in the S3 helix (Fig. 8 D). This resulted in a decreased distance between E208 and R219 (Figs. 8 E and 10 A). To measure the dynamics of the T207S mutation, we measured the dihedral angle between the atoms N, Cα, Cβ, and O (of the hydroxyl group) in T207 and T207S (Fig. 8 F). There were two peaks at around −50° and 60° with a slight preference for the latter in hNav1.5, corresponding to the hydroxyl group of T207 hydrogen bonding to the carboxyl oxygens of the E208 side chain and the methyl group in T207 facing away from the VSD interior (Fig. 8 G, right). In the T207S mutation, this interaction
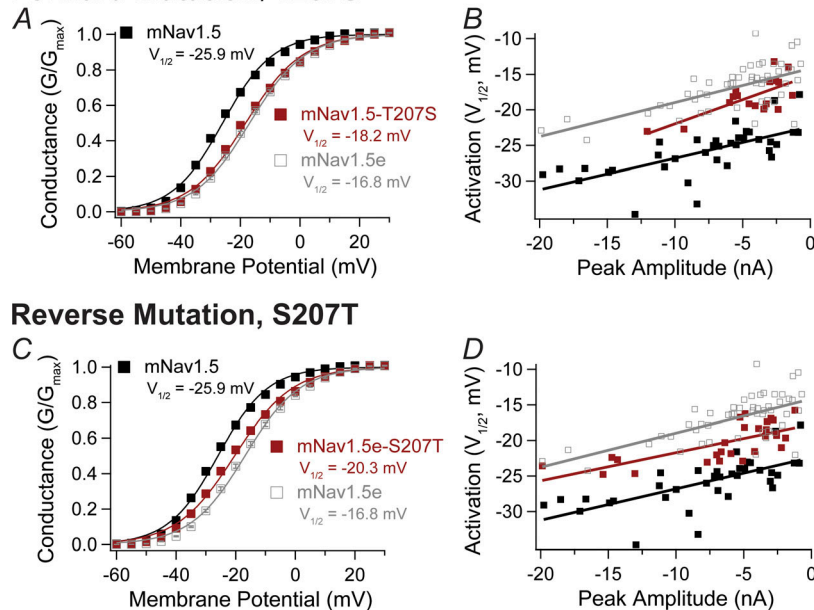
was depleted and instead the hydroxyl group favored hydrogen bonding to the backbone oxygen in M203 (Fig. 8 G, left), similar to the peak at −50° in hNav1.5.

Mutation of the DI S3–S4 linker similarly affects mNav1.4 channel gating
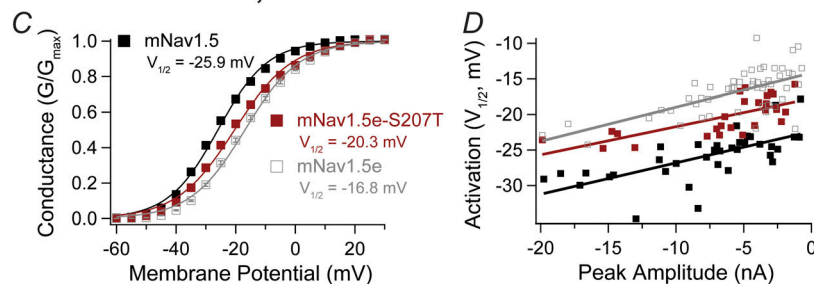
Although splicing in DI selectively alters the voltage dependence of activation in Nav1.5, this is not true in other tested isoforms, namely Nav1.1, Nav1.2, and Nav1.7 (Chatelier et al., 2008; Fletcher et al., 2011; Liavas et al., 2017). To determine whether Nav1.5 was unique in this respect, we mutated the two key residue exchanges at positions 207 and 211 of another isoform, mNav1.4 (Fig. 11). We chose mNav1.4 because of its distinctive phylogenetic relationship compared with other Nav channel isoforms that have been studied (Goldin et al., 2000). To date, alternative splicing of the mNav1.4 gene has not been reported (Loussouarn et al., 2015).

mNav1.4 expressed poorly in HEK-293T cells when transfected alone. However, when cotransfected with the auxiliary subunit β3, the number of cells expressing mNav1.4 and their peak amplitudes increased appreciably. We were mindful of the fact that β3 might impact the effect of DI S3–S4 splicing. Consequently, as a control, we verified that the gating shifts observed

Forward Mutation, T207S
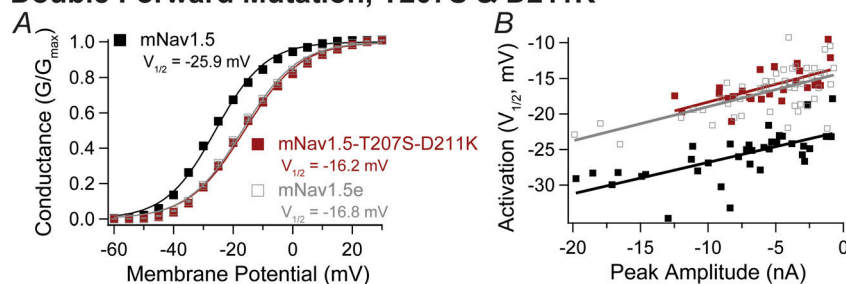

Reverse Mutation, S207T

Figure 4. **The threonine-serine switch at position 207 also influences channel activation. (A)** Introducing T207S into mNav1.5 also causes a shift in the activation profile toward that of mNav1.5e. The activation $V_{1/2}$ of mNav1.5-T207S (red) was −18.2 ± 0.64 mV (n = 17), distinct from mNav1.5 (P < 0.001) and apparently overlapping with mNav1.5e (P = 0.30). The slope factor k was 9.3 ± 0.15. **(B)** The y-intercept of the mNav1.5-T207S scatter measured −15.2 ± 0.21 mV, falling between mNav1.5 (P < 0.001) and mNav1.5e (P < 0.05). The regression line slope was steeper than usual, at 0.68 ± 0.04 mV/nA. **(C)** Replacing S207T in mNav1.5e produces an intermediate phenotype in terms of channel activation. The activation $V_{1/2}$ of mNav1.5e-S207T (red) was −20.3 ± 0.53 mV (n = 26), distinct from both mNav1.5e (P < 0.001) and mNav1.5 (P < 0.001). The slope factor k was 9.6 ± 0.14. **(D)** The y-intercept of the mNav1.5e-S207T scatter measured −17.7 ± 0.13 mV, different from both mNav1.5 (P < 0.001) and mNav1.5e (P < 0.001). The regression line slope was 0.40 ± 0.02 mV/nA.

between mNav1.5 and mNav1.5e persisted when co-expressed with β3. As anticipated, the 10 mV shift in channel activation was preserved between mNav1.5 ($V_{1/2}$, −25.9 ± 0.55 mV, n = 11) and mNav1.5e ($V_{1/2}$, −13.8 ± 0.76, n = 18, P < 0.001) when co-expressed with β3 (Table 1). Steady-state inactivation between both isoforms was similar ($V_{1/2}$ of mNav1.5 + β3 of −76.3 ± 0.66 mV, n = 12, and $V_{1/2}$ of mNav1.5e of −74.5 ± 0.55 mV, n = 17, P < 0.05, Table 2) and recovery from inactivation was statistically indistinguishable (weighted τ of mNav1.5 + β3 of 5.2 ± 0.46 ms, n = 12, and weighted τ of mNav1.5e + β3 of 4.9 ± 0.24 ms, n = 15, P = 0.54, Table 2). We therefore concluded that co-expression with β3 does not impact the ability of alternative splicing to alter channel gating.

Cotransfection of mNav1.4 with β3 generated membrane currents that activated at potentials more depolarized than Nav1.5, with $V_{1/2}$ values of −2.3 ± 0.65 mV (n = 13, Fig. 11, B and C). The primary sequence of mNav1.4 contains Thr at position 207 and Asp at position 211, similar to mNav1.5 (Fig. 11 A). Therefore, to modify mNav1.4 channel gating behavior to mimic that of mNav1.5e, we introduced serine and lysine into positions 207 and 211, respectively. The conductance–voltage relationship of mNav1.4-T207S-D211K + β3 was significantly right-shifted relative to mNav1.4 + β3, with a $V_{1/2}$ of 5.7 ± 0.50 mV (n = 25, P < 0.001; Fig. 11 C and Table 1). The difference was specific to channel activation, with no effect on steady-state inactivation ($V_{1/2}$ mNav1.4 + β3 of −55.8 ± 0.66 mV, n = 13, and $V_{1/2}$ mNav1.4-

Double Forward Mutation, T207S & D211K
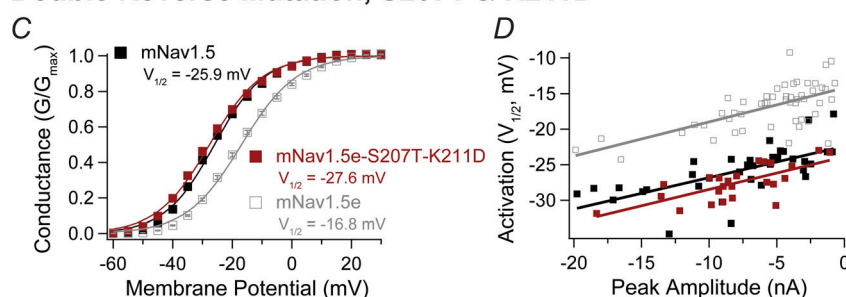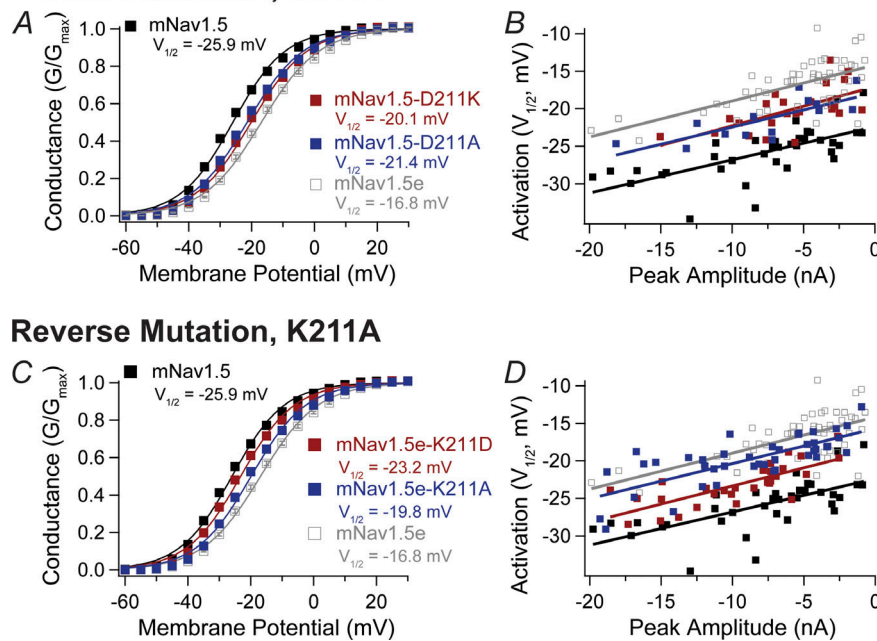

Double Reverse Mutation, S207T & K211D

Figure 5. **Combined, the Thr/Ser and Asp/Lys switches account for the full gating difference between mNav1.5 and mNav1.5e. (A)** Introducing both T207S and D211K into mNav1.5 results in an activation profile that is indistinguishable from that of mNav1.5e. The activation $V_{1/2}$ of mNav1.5-T207S-D211K (red) was −16.2 ± 0.50 mV (n = 25), overlapping with mNav1.5e (P = 0.64) yet distinct from mNav1.5 (P < 0.001). The slope factor k was 9.3 ± 0.10. **(B)** The y-intercept of the mNav1.5-T207S-D211K scatter measured −13.3 ± 0.16 mV, coinciding with mNav1.5e (P = 0.43) but remaining distinct from mNav1.5 (P < 0.001). The regression line slope was 0.50 ± 0.02 mV/nA. **(C)** Replacing both S207T and K211D in mNav1.5e produces a phenotype similar to that of mNav1.5. The activation $V_{1/2}$ of mNav1.5e-S207T-K211D (red) was −27.6 ± 0.51 mV (n = 24), distinct from mNav1.5e (P < 0.001) yet identical to mNav1.5 (P = 0.10). The slope factor k was 8.8 ± 0.16. **(D)** The y-intercept of the mNav1.5e-S207T-K211D scatter measured −23.9 ± 0.17 mV, overshooting mNav1.5 in the negative direction (P < 0.05) yet still very distinct from mNav1.5e (P < 0.001). The regression line slope was 0.46 ± 0.02 mV/nA.

Forward Mutation, D211A
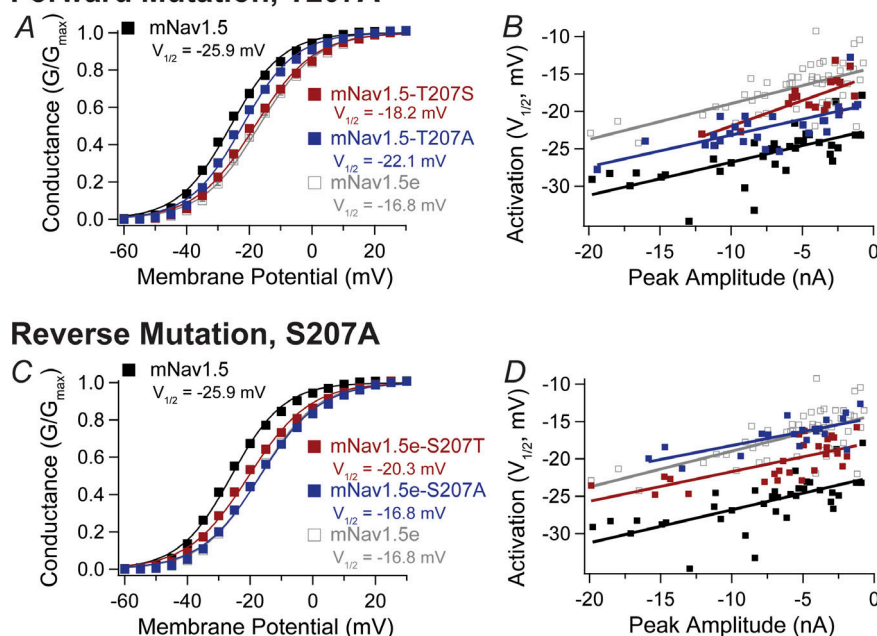

Reverse Mutation, K211A

Figure 6. **The presence of a negative charge at position 211 is essential to the hyperpolarized gating profile of mNav1.5. (A)** Introducing D211A in mNav1.5 results in an activation profile that is indistinguishable from the mutant mNav1.5-D211K, as if loss of the negative charge were more critical to the altered gating shift than gaining the positive charge. The activation $V_{1/2}$ of mNav1.5-D211A (blue) was −21.4 ± 0.75 mV (n = 14), similar to mNav1.5-D211K (red, P = 0.64). The slope factor k was 8.8 ± 0.19. **(B)** The y-intercept of the mNav1.5-D211A scatter measured −17.9 ± 0.07 mV, coinciding with mNav1.5-D211K (P = 0.92). The regression line slope was 0.46 ± 0.01 mV/nA. **(C)** Substituting K211A in mNav1.5e also produces a small but nonnegligible shift, taking on a phenotype between mNav1.5e-K211D and mNav1.5e, suggesting that the presence of the positive charge may matter to a limited degree. The activation $V_{1/2}$ of mNav1.5e-K211A (blue) was −19.8 ± 0.50 mV (n = 42), distinct from both mNav1.5e-K211D (red, P < 0.001) and mNav1.5e (P < 0.001). The slope factor k was 8.5 ± 0.18. **(D)** The y-intercept of the mNav1.5e-K211A scatter measured −15.7 ± 0.07 mV, distinct from both mNav1.5e-K211D (P < 0.001) and mNav1.5e (P < 0.05). The regression line slope was 0.47 ± 0.01 mV/nA.

T207S-D211K + β3 of −55.3 ± 0.36 mV, n = 21; P = 0.53; Fig. 11, E and F; and Table 2) and recovery from inactivation (weighted τ mNav1.4 + β3 of 1.23 ± 0.18 ms, n = 12, and weighted τ of mNav1.4-T207S-D211K + β3, 1.04 ± 0.07 ms, n = 17, P = 0.34; Fig. 11 G and Table 2). This observation demonstrates that the two key residues in DI of Nav1.5 that establish the channel activation profile are transferable to other Nav channel family members.

Discussion

The present study advances our understanding of Nav channel gating in several important ways. First, we show that differences in the activation properties of alternatively spliced isoforms of Nav1.5 are mediated equally by two amino acid residues in the S3–S4 linker of DI. Second, our electrophysiological data and MD simulations suggest that these residues act through distinct structural mechanisms to modify movement of the voltage

Forward Mutation, T207A

Reverse Mutation, S207A

Figure 7. **A constrained hydrogen bond donor is required at position 207 to yield the hyperpolarized activation parameters of mNav1.5. (A)** Introducing T207A in mNav1.5 results in an activation profile that is also depolarized compared with mNav1.5, suggesting that the rigidity of the residue at this position is critical to the altered gating behavior. The activation $V_{1/2}$ of mNav1.5-T207A (blue) was −22.1 ± 0.56 mV (n = 26), distinct from mNav1.5 (P < 0.001). Admittedly, though, the shift is not as strong as that of mNav1.5-T207S (red, P < 0.001). The slope factor k was 8.3 ± 0.13. **(B)** The y-intercept of the mNav1.5-T207A scatter measured −18.9 ± 0.16 mV, distinct from both with mNav1.5 (P < 0.001) and mNav1.5-T207S (P < 0.01). The regression line slope was 0.42 ± 0.02 mV/nA. **(C)** Substituting S207A in mNav1.5e had virtually no effect, highlighting the importance of losing the sterically constrained threonine residue in causing the shift in channel activation. The activation $V_{1/2}$ of mNav1.5e-S207A (blue) was −16.8 ± 0.49 mV (n = 20), coinciding with mNav1.5e (P = 1.00). The slope factor k was 9.5 ± 0.11. **(D)** The y-intercept of the mNav1.5e-S207A scatter measured −14.5 ± 0.14 mV, indistinguishable from mNav1.5e (P = 0.95). The regression line slope was 0.37 ± 0.02 mV/nA.
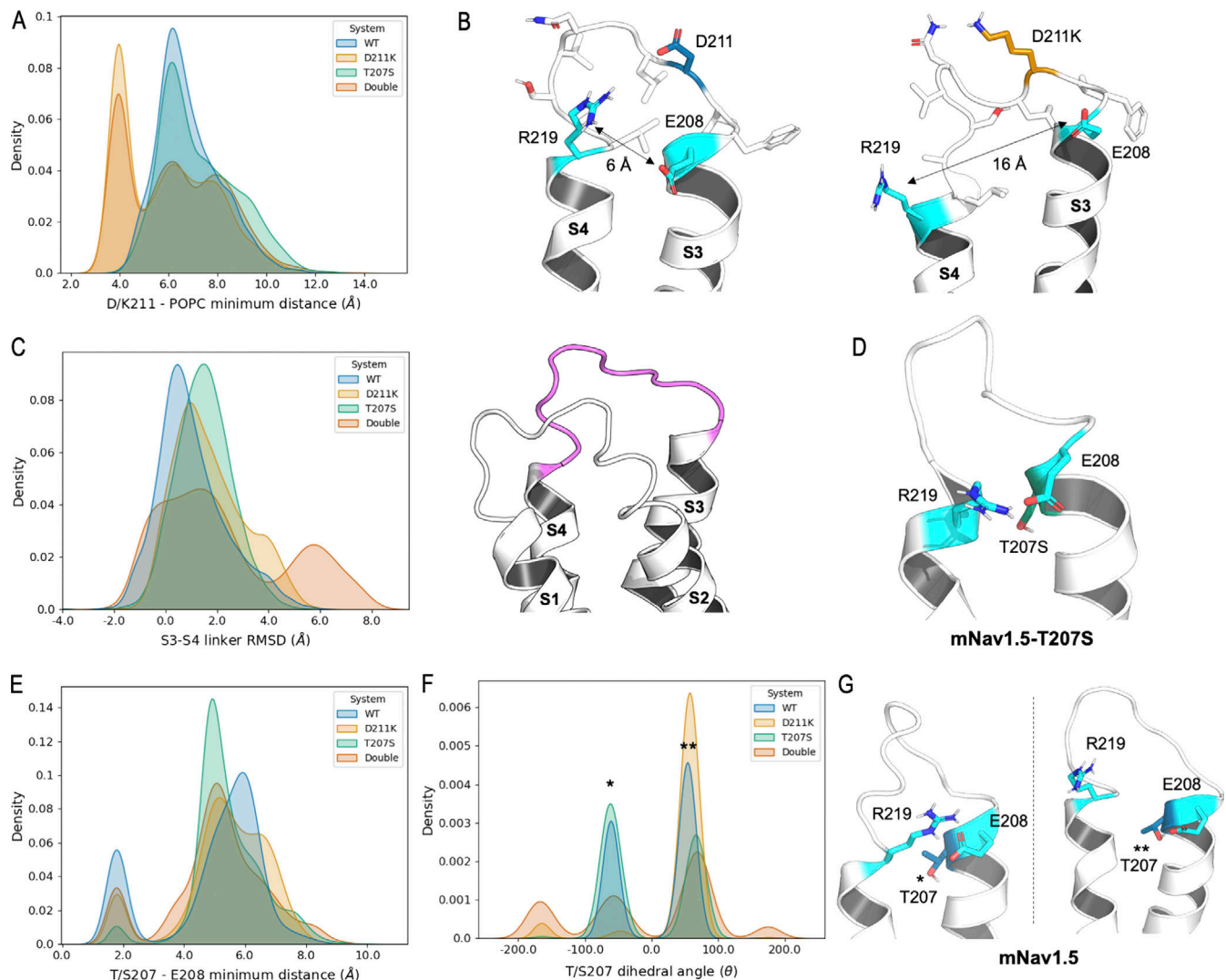
Figure 8. **Molecular dynamics simulations of hNav1.5 and hNav1.5-D211K/T207S reveal disruptions within the VSD of DI in Nav1.5. (A)** Minimum distance between D/K211 and POPC lipid head groups. The distances were calculated between the center of geometry of terminal side chain atoms (see http://github.com/bigginlab/nav-alt-splice for full definitions). **(B)** Representative snapshot of the S3–S4 linker containing D211 (dark blue) in the hNav1.5 VSD (left) and pronounced distortion with the D211K mutation (orange). The distance between E208 and R219 (cyan) at the top of the VSD increase in the presence of D211K (black arrow). **(C)** RMSD of the S3–S4 linker (magenta). **(D)** Snapshot of the decreased distance between E208 and R219 (cyan) due to the T207S mutation (dark green). **(E)** Minimum distance between the hydroxyl hydrogen in T/S207 and the carboxyl group oxygens in E208. **(F)** Dihedral angle between N, Cα, Cβ, and O (of the hydroxy group) atoms in T/S207. **(G)** Representative snapshots of T207 hNav1.5 conformations (dark blue) at the two main dihedral angle peaks (indicated by asterisks in F). The hydroxyl hydrogen interacts with the carbonyl backbone (single asterisks) of M208 and the carboxyl group of E208 (double asterisks).

sensor and thus impact channel gating. Third and finally, mutation of the homologous residues in skeletal muscle Nav1.4 channels elicits a similar shift in channel activation, suggesting that the overall architecture of the S3–S4 linker of DI and how it interacts with other amino acid residues may be shared among other Nav channel family members.

Critical roles of alternatively spliced residues in the DI voltage sensor

The ability of Nav channels to sense and respond to changes in membrane potential is conferred, in large part, by the gating charges in the S4 helix of each domain (Catterall, 2010). However, the S4 helix does not function in isolation, as the rest of the VSD plays a key role in shaping S4 movement. For example,

negatively charged residues on the S2 helix stabilize S4 gating charges in both the resting and activated states (DeCaen et al., 2008; DeCaen et al., 2009; Yarov-Yarovoy et al., 2012), and the hydrophobicity of residues on the S2 and S4 helices can modulate the rate at which the S4 helix changes conformation (Lacroix et al., 2013).

Alternatively spliced residues in the DI S3–S4 extracellular linker influence channel activation in a similar allosteric manner. Thr207 and Asp211 in mNav1.5 sit atop the S3 segment and the center of the S3–S4 extracellular loop, respectively, yet they impact the downstream S4 helix by facilitating its translocation at more hyperpolarized potentials. In contrast, mutations T207S and D211K in mNav1.5 hinder S4 translocation, as evidenced by the 10-mV depolarizing shift in the mutant channel's conductance–voltage profile. While the importance of the
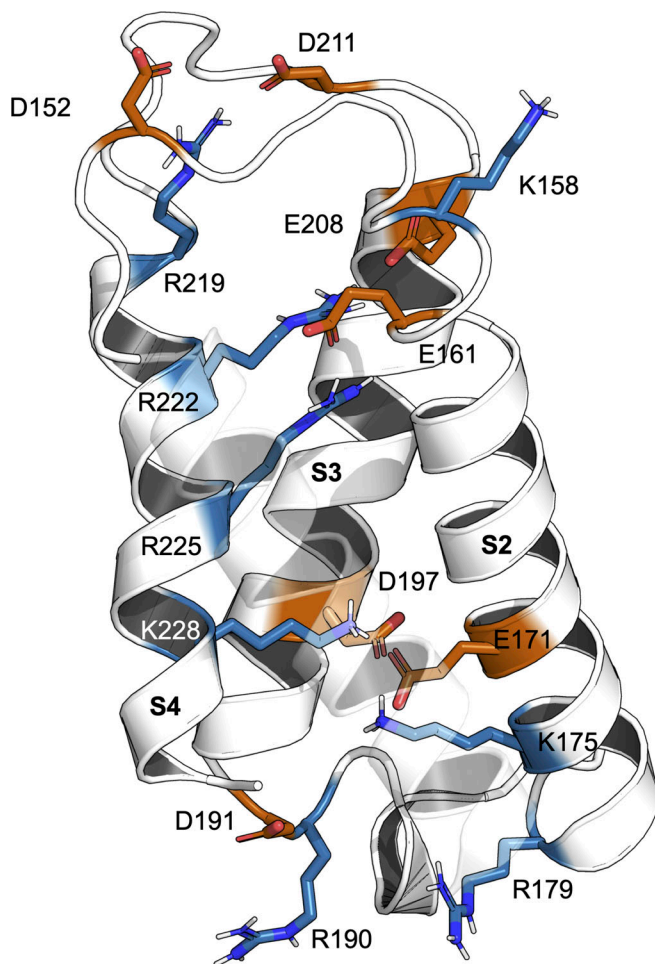
Figure 9. **Overview of key charged residues present within the VSD.** The VSD of D1 in mNav1.5. The VSD (white) contains four transmembrane helices (S1–S4, labeled in bold) with a number of positively (blue) and negatively (orange) charged residues that make up critical salt bridges during S4 translocation during mNav1.5 depolarization. Note that the S1 label has been removed and the helix shown as transparent for clarity.

exchange at position 211 to the altered activation phenotype was previously reported (Onkal et al., 2008), the role of the switch at position 207 has not been identified until now.

Using MD, we further probed the mechanism by which residue exchanges at positions 207 and 211 alter channel activation. We uncovered that the T207S mutation in hNav1.5 changes hydrogen bond networks embedded within the VSD that disrupt key salt-bridge interactions (in particular E208/R219), whereas the D211K mutation increases the likelihood for the channel to interact with the surrounding plasma membrane and distorts the S3–S4 linker. We predict that these conformational changes most likely destabilize the VSD in such a way that more energy is required to induce conformational changes therein. We propose that these structural distinctions explain the shift in activation threshold that is observed between neonatal and adult splice-forms of Nav1.5.

DI is preferentially targeted by alternative splicing
The DI S3–S4 extracellular linker is a site that is regularly modified by mutually exclusive exon splicing. To date, six of the

nine existing mammalian isoforms that are regulated by alternative splicing at this site include Nav1.1, Nav1.2, Nav1.3, Nav1.5, Nav1.6, and Nav1.7 (Schroeter et al., 2010; Fletcher et al., 2011). Interestingly, in this study, we show that the functional properties of Nav1.4 have the capacity to be regulated through the same changes in amino acid sequence, even though the SCN4A gene is not actually subject to alternative splicing in skeletal muscle (Loussouarn et al., 2015). It is curious that, when comparing alternative splicing across all Nav channel isoforms, DI is more robustly regulated than DII, DIII, and DIV. As discussed in more detail below, the greater frequency of alternative splicing in DI identifies it as a region of the Nav channel that may have a more privileged role in dictating channel gating.

The canonical view of Nav channel gating purports that movement of DI, DII, and DIII give rise to channel activation, whereas movement of DIV initiates the onset of inactivation (Ahern et al., 2016). An added distinction is that DI, DII, and DIII may not contribute equally to channel activation. For example, VCF studies have revealed that the upward displacement of the VSD of DI through to DIII activate at different membrane potentials, with movement in DIII occurring first followed by DI and then DII at more depolarized potentials (Chanda and Bezanilla, 2002; Varga et al., 2015). In addition, charge-neutralization of the voltage sensor of DI causes a significant hyperpolarizing shift in channel activation compared with DII and III of Nav1.4 (Capes et al., 2013) and Nav1.5 (Brake et al., 2021 Preprint), which may suggest that movement of DI is the rate-limiting step for channel activation, at least for these Nav channel isoforms. Interestingly, however, DI S3–S4 splicing in Nav1.1, Nav1.2, and Nav1.7 reveals that DI may play a more dominant role in inactivation (Fletcher et al., 2011; Liavas et al., 2017), suggesting that DI fulfills different roles amongst these Nav channel isoforms. Taken together, these studies further underline the importance of DI as a target for alternate splicing given its pivotal role in shaping both channel activation and inactivation.

Physiological roles of alternative splicing of Nav channels
The physiological role of alternative splicing of DI is not fully resolved. Interestingly however, neonatal transcripts are highly expressed in excitable tissues before birth, whereas the adult isoforms dominate expression in postnatal tissue (Sarao et al., 1991; Yarowsky et al., 1991; Gustafson et al., 1993; Chioni et al., 2005; Gazina et al., 2010; Liang et al., 2021). In the case of the cardiac channel, Nav1.5, it is unclear why the developing heart would favor a channel that requires stronger depolarizations to promote channel activation. Interestingly, the neonatal heart has been shown to be less excitable than the adult heart (Gomes et al., 2002), consistent with expression of a Nav channel with a higher activation threshold. However, these differences in the neonatal and adult heart rates have been largely explained by other voltage-gated calcium and potassium channels (Wang and Sobie, 2008). Accordingly, more work is still needed to better delineate between the contribution of different ion channel families. Unlike Nav1.5, neonatal isoforms of neuronal Nav1.1, Nav1.2, and Nav1.7 recover more efficiently from inactivation (with one possible exception for Nav1.2; see Thompson et al., 2020). This may offset the stronger drive toward channel inactivation in neonatal tissue, given that developing neurons often have more depolarized resting membrane
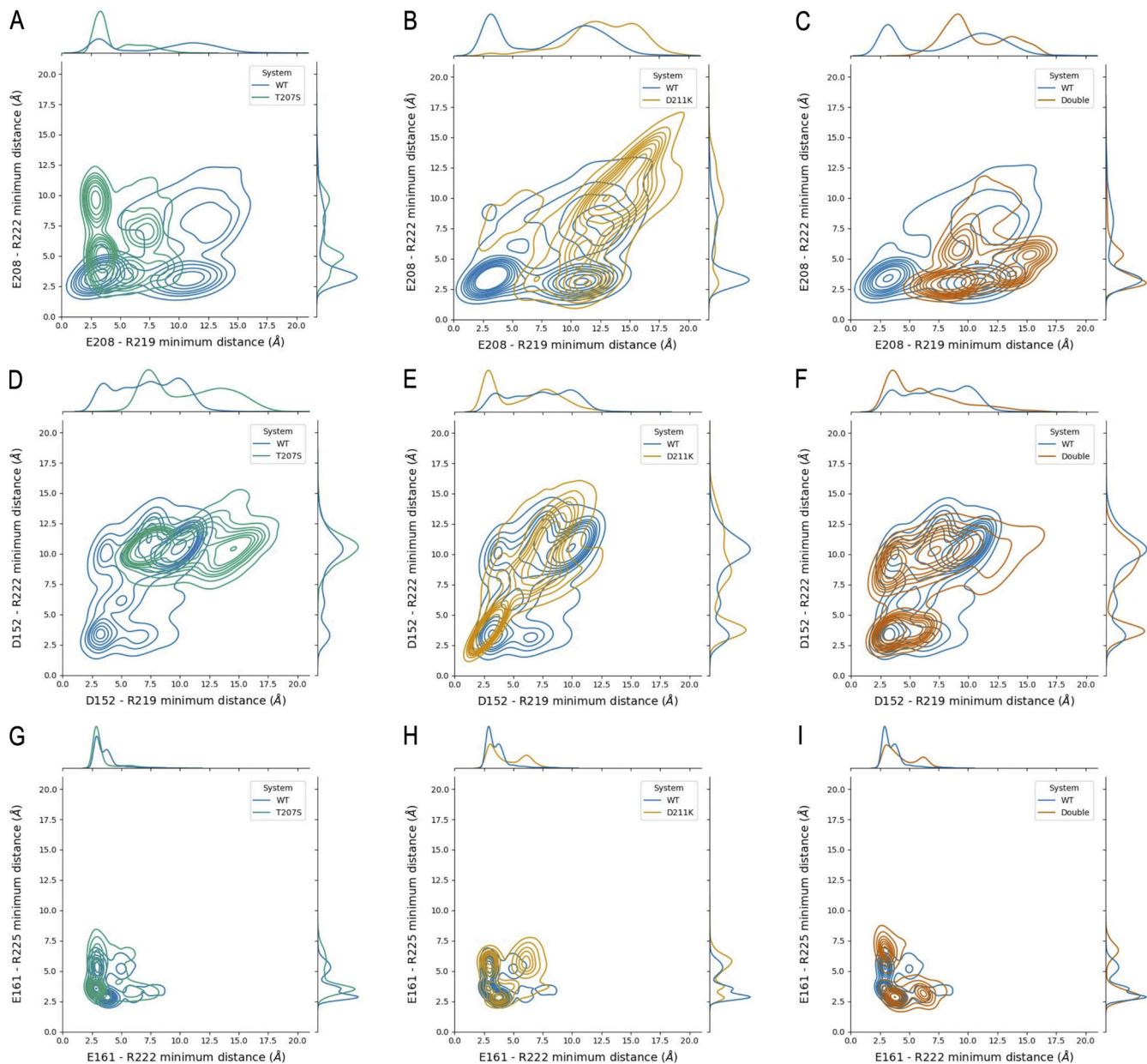
Figure 10. **2-D joint plots of salt-bridge distances in the VSD.** Minimum distances between two residues in the VSD. Distances were measured from the center of geometry of carboxyl oxygen atoms in glutamic/aspartic acid and the terminal –NH$_2$ atoms in the guanidino group. See http://github.com/bigginlab/nav-alt-splice for full atom selections. **(A–C)** Minimum distances between E208/R222 and E208/R219 for hNav1.5-T207S, hNav1.5-D211K, and hNav1.5-T207S-D211K, respectively. **(D–F)** Minimum distances between D152/R222 and D152/R219 for hNav1.5-T207S, hNav1.5-D211K, and hNav1.5-T207S-D211K, respectively. **(G–I)** Minimum distances between E161/R225 and E161/R222 for hNav1.5-T207S, hNav1.5-D211K, and hNav1.5-T207S-D211K, respectively.

potentials than their adult counterparts (Tyzio et al., 2003). While their exact roles in vivo remain to be elucidated, the effects of DI S3–S4 splicing are predicted to have important impacts on cell firing. Adjusting the ratio of neonatal to adult Nav1.2 expression, for example, can alter the rate of action potential generation in computational models (Thompson et al., 2020). In addition, transfection of different Nav1.1 splice variants into cultured hippocampal neurons determines the maximum firing rate of trains of action potentials (Lignani et al., 2020 *Preprint*).

While the role of DI alternative splicing in physiology remains an active area of investigation, it is clear that dysregulated

splicing is involved in a number of disease states. In kainate-induced seizure models of the hippocampus, there is an upregulation of neonatal Nav1.2 and Nav1.3 transcripts (Bartolomei et al., 1997). Consistent with this, mice modified to exclusively express the adult form of Nav1.2 displayed increased seizure susceptibility (Gazina et al., 2015). In the heart, neonatal Nav1.5 was shown to be upregulated in the adult hearts of individuals with myotonic dystrophy (Wahbi et al., 2013; Freyermuth et al., 2016). Moreover, biasing splicing to increase the proportion of neonatal Nav1.5 in adult tissues was shown even to promote heart arrhythmias and cardiac conduction delay in mice (Freyermuth
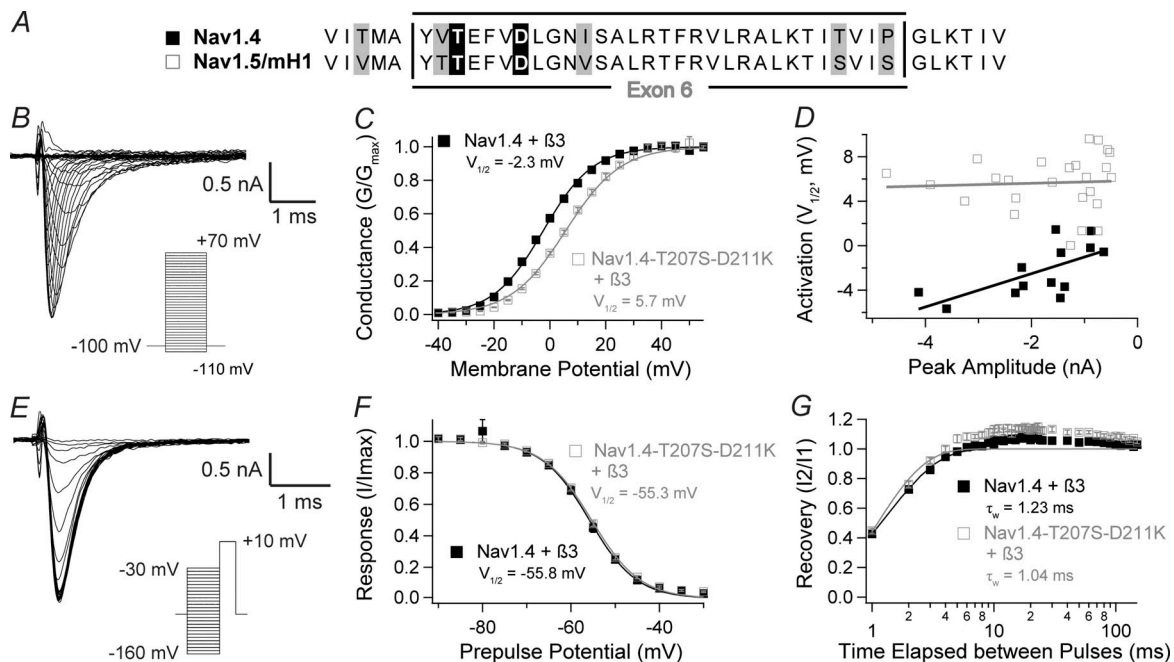
Figure 11.   **The ability for the DI S3–S4 linker to alter channel activation is conserved in mNav1.4. (A)** Sequence alignment of mouse Nav1.4 and Nav1.5, in the adult splice form, in the regions of and surrounding exon 6. mNav1.5 and mNav1.4 are largely similar in sequence, with the exception of those amino acid differences shaded in gray. The black boxes highlight the Thr207 and Asp211 that were shown to be important in exon 6 splicing of Nav1.5 and that are also conserved in mNav1.4. **(B)** Sample current traces elicited by the mNav1.4 + β3 complex during an activation protocol. Cells were stepped from −100 mV to a range of membrane potentials between −110 mV and +70 mV, in increments of 5 mV. **(C)** Activation profiles of mNav1.4 + β3 (black) and the double mutant mNav1.4-T207S-D211K + β3 (gray) recapitulate the ~10-mV shift in channel activation, as seen in Nav1.5. $V_{1/2}$ values of mNav1.4-T207S-D211K + β3 and mNav1.4 + β3 were 5.7 ± 0.50 mV ($n = 25$) and −2.3 ± 0.65 mV ($n = 13$, P < 0.001), respectively. The k values were 9.0 ± 0.24 and 8.8 ± 0.21, respectively (P = 0.51). **(D)** Distributions of activation $V_{1/2}$ plotted against peak current amplitude demonstrate the difference in activation profiles of mNav1.4-T207S-D211K + β3 and mNav1.4 + β3. Regression line y-intercepts of mNav1.4-T207S-D211K + β3 and mNav1.4 + β3 were 5.9 ± 0.18 and 0.48 ± 0.31 mV, respectively (P = 0.38). Regression line slopes were parallel, at 0.12 ± 0.02 and 1.4 ± 0.14 mV/nA (P = 0.11). **(E)** Sample current traces elicited by mNav1.4 + β3 during a steady-state inactivation protocol. Cells were given a variable pre-pulse potential, ranging from −160 to −30 mV in increments of 5 mV, and then stepped to +10 mV to evoke a current response. **(F)** Inactivation profiles of mNav1.4-T207S-D211K + β3 and mNav1.4 + β3 show that the two variants do not differ in terms of steady-state inactivation. $V_{1/2}$ values were −55.3 ± 0.36 ($n = 21$) and −55.8 ± 0.66 mV ($n = 13$) for mNav1.4-T207S-D211K and mNav1.4 + β3, respectively (P = 0.53). k values were −5.4 ± 0.15 and −5.3 ± 0.20 for mNav1.4-T207S-D211K and mNav1.4 + β3, respectively (P = 0.59). **(G)** mNav1.4-T207S-D211K + β3 and mNav1.4 + β3 do not differ in terms of recovery from inactivation either. The fraction of Nav channels recovered was plotted against the interpulse interval and fitted to a double exponential function, yielding weighted τ values of 1.04 ± 0.07 ($n = 17$) and 1.23 ± 0.18 ms ($n = 12$) for mNav1.4-T207S-D211K + β3 and mNav1.4 + β3, respectively (P = 0.34).

et al., 2016). Finally, studies of recombinant channels suggest that splicing in the DI S3–S4 linker can alter the gating and pharmacology of disease mutants of Nav1.2 and Nav1.7, which may explain the observed epileptic and hyperalgesic phenotypes (Jarecki et al., 2009; Choi et al., 2010; Liao et al., 2010; Thompson et al., 2020). Taking these findings together, while alternative splicing in DI may serve as an important mechanism for fine-tuning the activity of excitable cells, regulation must be kept under control to circumvent debilitating imbalances in cellular excitability.

Acknowledgments

References

Abraham, M., T. Murtola, R. Schulz, S. Páll, J. Smith, B. Hess, and E. Lindahl. 2015. GROMACS: high performance molecular simulations through multi-level parallelism from laptops to supercomputers. *SoftwareX*. 1-2: 19–25. https://doi.org/10.1016/j.softx.2015.06.001

Ahern, C.A., J. Payandeh, F. Bosmans, and B. Chanda. 2016. The hitchhiker's guide to the voltage-gated sodium channel galaxy. *J. Gen. Physiol.* 147: 1–24. https://doi.org/10.1085/jgp.201511492

Bartolomei, F., M. Gastaldi, A. Massacrier, R. Planells, S. Nicolas, and P. Cau. 1997. Changes in the mRNAs encoding subtypes I, II and III sodium channel alpha subunits following kainate-induced seizures in rat brain. *J. Neurocytol.* 26:667–678. https://doi.org/10.1023/a:1018549928277

Berendsen, H.J.C., J.P.M Postma, W.F. Vangunsteren, A. Dinola, and J.R. Haak. 1984. Molecular-dynamics with coupling to an external bath. *J. Chem. Phys.* 81:3684–3690. https://doi.org/10.1063/1.448118

Best, R.B., and G. Hummer. 2009. Optimized molecular dynamics force fields applied to the helix-coil transition of polypeptides. *J. Phys. Chem. B.* 113: 9004–9015. https://doi.org/10.1021/jp901540t

Brake, N., A.S. Mancino, Y. Yan, T. Shimomura, H. Silveira, Y. Kubo, A. Khadra, and D. Bowie. 2021. Intrinsic gating behavior of voltage-gated sodium channels predetermines regulation by auxiliary β-subunits. *bioRxiv.* https://doi.org/10.1101/2021.02.25.432706 (Preprint posted February 25 2021)

Braman, J., C. Papworth, and A. Greener. 1996. Site-directed mutagenesis using double-stranded plasmid DNA templates. *Methods Mol. Biol.* 57: 31–44. https://doi.org/10.1385/0-89603-332-5:31

Camacho, J.A., S. Hensellek, J.S. Rougier, S. Blechschmidt, H. Abriel, K. Benndorf, and T. Zimmer. 2006. Modulation of Nav1.5 channel function by an alternatively spliced sequence in the DII/DIII linker region. *J. Biol. Chem.* 281:9498–9506. https://doi.org/10.1074/jbc.M509716200

Capes, D.L., M.P. Goldschen-Ohm, M. Arcisio-Miranda, F. Bezanilla, and B. Chanda. 2013. Domain IV voltage-sensor movement is both sufficient and rate limiting for fast inactivation in sodium channels. *J. Gen. Physiol.* 142:101–112. https://doi.org/10.1085/jgp.201310998

Catterall, W.A... 2010. Ion channel voltage sensors: structure, function, and pathophysiology. *Neuron.* 67:915–928. https://doi.org/10.1016/j.neuron.2010.08.021

Catterall, W.A. 2012. Voltage-gated sodium channels at 60: structure, function and pathophysiology. *J. Physiol.* 590:2577–2589. https://doi.org/10.1113/jphysiol.2011.224204

Chanda, B., and F. Bezanilla. 2002. Tracking voltage-dependent conformational changes in skeletal muscle sodium channel during activation. *J. Gen. Physiol.* 120:629–645. https://doi.org/10.1085/jgp.20028679

Chatelier, A., L. Dahllund, A. Eriksson, J. Krupp, and M. Chahine. 2008. Biophysical properties of human Na v1.7 splice variants and their regulation by protein kinase A. *J. Neurophysiol.* 99:2241–2250. https://doi.org/10.1152/jn.01350.2007

Chioni, A.M., S.P. Fraser, F. Pani, P. Foran, G.P. Wilkin, J.K. Diss, and M.B. Djamgoz. 2005. A novel polyclonal antibody specific for the Na$_v$1.5 voltage-gated Na$^+$ channel 'neonatal' splice form. *J. Neurosci. Methods.* 147:88–98. https://doi.org/10.1016/j.jneumeth.2005.03.010

Choi, J.S., X. Cheng, E. Foster, A. Leffler, L. Tyrrell, R.H.M. Te Morsche, E.M. Eastman, H.J. Jansen, K. Huehne, C. Nau, et al. 2010. Alternative splicing may contribute to time-dependent manifestation of inherited erythromelalgia. *Brain.* 133:1823–1835. https://doi.org/10.1093/brain/awq114

Copley, R.R. 2004. Evolutionary convergence of alternative splicing in ion channels. *Trends Genet.* 20:171–176. https://doi.org/10.1016/j.tig.2004.02.001

Darden, T., D. York, and L. Pedersen. 1993. Particle Mesh Ewald - an N.Log(N) method for Ewald sums in large systems. *J. Chem. Phys.* 98:10089–10092. https://doi.org/10.1063/1.464397

DeCaen, P.G., V. Yarov-Yarovoy, E.M. Sharp, T. Scheuer, and W.A. Catterall. 2009. Sequential formation of ion pairs during activation of a sodium channel voltage sensor. *Proc. Natl. Acad. Sci. USA.* 106:22498–22503. https://doi.org/10.1073/pnas.0912307106

DeCaen, P.G., V. Yarov-Yarovoy, Y. Zhao, T. Scheuer, and W.A. Catterall. 2008. Disulfide locking a sodium channel voltage sensor reveals ion pair formation during activation. *Proc. Natl. Acad. Sci. USA.* 105:15142–15147. https://doi.org/10.1073/pnas.0806486105

Edelheit, O., A. Hanukoglu, and I. Hanukoglu. 2009. Simple and efficient site-directed mutagenesis using two single-primer reactions in parallel to generate mutants for protein structure-function studies. *BMC Biotechnol.* 9:61. https://doi.org/10.1186/1472-6750-9-61

Essmann, U., L. Perera, M.L. Berkowitz, T. Darden, H. Lee, and L.G. Pedersen. 1995. A smooth particle mesh Ewald method. *J. Chem. Phys.* 103: 8577–8593. https://doi.org/10.1063/1.470117

Fletcher, E.V., D.M. Kullmann, and S. Schorge. 2011. Alternative splicing modulates inactivation of type 1 voltage-gated sodium channels by toggling an amino acid in the first S3-S4 linker. *J. Biol. Chem.* 286: 36700–36708. https://doi.org/10.1074/jbc.M111.250225

Freyermuth, F., F. Rau, Y. Kokunai, T. Linke, C. Sellier, M. Nakamori, Y. Kino, L. Arandel, A. Jollet, C. Thibault, et al. 2016. Splicing misregulation of SCN5A contributes to cardiac-conduction delay and heart arrhythmia in myotonic dystrophy. *Nat. Commun.* 7:11067. https://doi.org/10.1038/ncomms11067

Gazina, E.V., B.T.W Leaw, K.L. Richards, V.C. Wimmer, T.H. Kim, T.D. Aumann, T.J. Featherby, L. Churilov, V.E. Hammond, C.A. Reid, and S. Petrou. 2015. 'Neonatal' Nav1.2 reduces neuronal excitability and affects seizure susceptibility and behaviour. *Hum. Mol. Genet.* 24:1457–1468. https://doi.org/10.1093/hmg/ddu562

Gazina, E.V., K.L. Richards, M.B.C Mokhtar, E.A. Thomas, C.A. Reid, and S. Petrou. 2010. Differential expression of exon 5 splice variants of sodium channel alpha subunit mRNAs in the developing mouse brain. *Neuroscience.* 166:195–200. https://doi.org/10.1016/j.neuroscience.2009.12.011

Goldin, A.L. 2002. Evolution of voltage-gated Na$^+$ channels. *J. Exp. Biol.* 205: 575–584. https://doi.org/10.1242/jeb.205.5.575

Goldin, A.L., R.L. Barchi, J.H. Caldwell, F. Hofmann, J.R. Howe, J.C. Hunter, R.G. Kallen, G. Mandel, M.H. Meisler, Y.B. Netter, et al. Nomenclature of voltage-gated sodium channels. *Neuron.* 28:365–368. https://doi.org/10.1016/s0896-6273(00)00116-1

Gomes, P.A.P., K.M. de Galvao, and E.F. Mateus. 2002. Excitability of isolated hearts from rats during postnatal development. *J. Cardiovasc. Electrophysiol.* 13:355–360. https://doi.org/10.1046/j.1540-8167.2002.00355.x

Gustafson, T.A., E.C. Clevinger, T.J. O'Neill, P.J. Yarowsky, and B.K. Krueger. 1993. Mutually exclusive exon splicing of type III brain sodium channel alpha subunit RNA generates developmentally regulated isoforms in rat brain. *J. Biol. Chem.* 268:18648–18653

Hess, B., H. Bekker, H.J.C. Berendsen, and J.G.E.M. Fraaije. 1997. LINCS: a linear constraint solver for molecular simulations. *J. Comput. Chem.* 18: 1463–1472

Hoover, W.G... 1985. Canonical dynamics: equilibrium phase-space distributions. *Phys. Rev. A Gen. Phys.* 31:1695–1697. https://doi.org/10.1103/physreva.31.1695

Jämbeck, J.P.M, and A.P. Lyubartsev. 2012a. Derivation and systematic validation of a refined all-atom force field for phosphatidylcholine lipids. *J. Phys. Chem. B.* 116:3164–3179. https://doi.org/10.1021/jp212503e

Jämbeck, J.P.M, and A.P. Lyubartsev. 2012b. An extension and further validation of an all-atomistic force field for biological membranes. *J. Chem. Theor. Comput.* 8:2938–2948. https://doi.org/10.1021/ct300342n

Jämbeck, J.P.M, and A.P. Lyubartsev. 2013. Another piece of the membrane puzzle: extending slipids further. *J. Chem. Theor. Comput.* 9:774–784. https://doi.org/10.1021/ct300777p

Jarecki, B.W., P.L. Sheets, Y. Xiao, J.O. Jackson II, and T.R. Cummins. 2009. Alternative splicing of Na$_v$1.7 exon 5 increases the impact of the painful PEPD mutant channel I1461T. *Channels (Austin).* 3:259–267. https://doi.org/10.4161/chan.3.4.9341

Jiang, D., H. Shi, L. Tonggu, T.M. Gamal El-Din, M,J, Lenaeus, Y. Zhao, C. Yoshioka, N. Zheng, and W.A. Catterall. 2020. Structure of the cardiac sodium channel. *Cell.* 180:122–134.e10. https://doi.org/10.1016/j.cell.2019.11.041

Jo, S., X. Cheng, J. Lee, S. Kim, S.J. Park, D.S. Patel, A.H. Beaven, K.I. Lee, H. Rui, S. Park, et al. 2017. CHARMM-GUI 10 years for biomolecular modeling and simulation. *J. Comput. Chem.* 38:1114–1124. https://doi.org/10.1002/jcc.24660

Jordan, M., A. Schallhorn, and F.M. Wurm. 1996. Transfecting mammalian cells: optimization of critical parameters affecting calcium-phosphate precipitate formation. *Nucleic Acids Res.* 24:596–601. https://doi.org/10.1093/nar/24.4.596

Jorgensen, W.L., J. Chandrasekhar, J.D. Madura, R.W. Impey, and M.L. Klein. 1983. Comparison of simple potential functions for simulating liquid water. *J. Chem. Phys.* 79:926–935. https://doi.org/10.1063/1.445869

Lacroix, J.J., F.V. Campos, L. Frezza, and F. Bezanilla. 2013. Molecular bases for the asynchronous activation of sodium and potassium channels required for nerve impulse generation. *Neuron.* 79:651–657. https://doi.org/10.1016/j.neuron.2013.05.036

Li, Z., X. Jin, T. Wu, G. Huang, K. Wu, J. Lei, X. Pan, and N. Yan. 2021. Structural basis for pore blockade of the human cardiac sodium channel Nav 1.5 by the antiarrhythmic drug quinidine. *Angew. Chem. Int. Ed. Engl.* 60:11474–11480. https://doi.org/10.1002/anie.202102196

Liang, L., S.F.Darbandi, S. Pochareddy, F.O. Gulden, M.C. Gilson, B.K. Sheppard, A. Sahagun, J.-Y. An, D.M. Werling, J.L.R. Rubenstein, et al. 2021. Developmental dynamics of voltage-gated sodium channel isoform expression in the human and mouse brain. *Genome Med.* https://doi.org/10.1186/s13073-021-00949-0

Liao, Y., L. Deprez, S. Maljevic, J. Pitsch, L. Claes, D. Hristova, A. Jordanova, S. Ala-Mello, A. Bellan-Koch, D. Blazevic, et al. 2010. Molecular correlates of age-dependent seizures in an inherited neonatal-infantile epilepsy. *Brain.* 133:1403–1414. https://doi.org/10.1093/brain/awq057

Liavas, A., G. Lignani, and S. Schorge. 2017. Conservation of alternative splicing in sodium channels reveals evolutionary focus on release from inactivation and structural insights into gating. *J. Physiol.* 595:5671–5685. https://doi.org/10.1113/JP274693

Lignani, G., A. Liavas, D.M. Kullmann, and S. Schorge. 2020. Alternative splicing tunes sodium channels to support channel- and neuron-specific effects. *bioRxiv*. https://doi.org/10.1101/2020.09.30.320788 (Preprint posted October 01 2020)

Loussouarn, G., D. Sternberg, S. Nicole, C. Marionneau, F. Le Bouffant, G. Toumaniantz, J. Barc, O.A. Malak, V. Fressart, Y. Pereon, et al. 2015. Physiological and pathophysiological insights of Nav1.4 and Nav1.5 comparison. *Front. Pharmacol.* 6:314. https://doi.org/10.3389/fphar.2015.00314

Michaud-Agrawal, N., E.J. Denning, T.B. Woolf, and O. Beckstein. 2011. MDAnalysis: a toolkit for the analysis of molecular dynamics simulations. *J. Comput. Chem.* 32:2319–2327. https://doi.org/10.1002/jcc.21787

Montnach, J., M. Lorenzini, A. Lesage, I. Simon, S. Nicolas, E. Moreau, C. Marionneau, I. Baro, M. De Waard, and G. Loussouarn. 2021. Computer modeling of whole-cell voltage-clamp analyses to delineate guidelines for good practice of manual and automated patch-clamp. *Sci. Rep.* 11: 3282. https://doi.org/10.1038/s41598-021-82077-8

Noda, M., S. Shimizu, T. Tanabe, T. Takai, T. Kayano, T. Ikeda, H. Takahashi, H. Nakayama, Y. Kanaoka, N. Minamino, et al. 1984. Primary structure of Electrophorus electricus sodium channel deduced from cDNA sequence. *Nature.* 312:121–127. https://doi.org/10.1038/312121a0

Nosé, S. 1984. A unified formulation of the constant temperature molecular-dynamics methods. *J. Chem. Phys.* 81:511–519. https://doi.org/10.1063/1.447334

Onkal, R., J.H. Mattis, S.P. Fraser, J.K.J. Diss, D. Shao, K. Okuse, and M.B.A. Djamgoz. 2008. Alternative splicing of Nav1.5: an electrophysiological comparison of 'neonatal' and 'adult' isoforms and critical involvement of a lysine residue. *J. Cell Physiol.* 216:716–726. https://doi.org/10.1002/jcp.21451

Parrinello, M., and A. Rahman. 1981. Polymorphic transitions in single-crystals - a new molecular-dynamics method. *J. Appl. Phys.* 52:7182–7190. https://doi.org/10.1063/1.328693

Payandeh, J., T. Scheuer, N. Zheng, and W.A. Catterall. 2011. The crystal structure of a voltage-gated sodium channel. *Nature.* 475:353–358. https://doi.org/10.1038/nature10238

Qiao, M., and J.R. Sanes. 2015. Genetic method for labeling electrically coupled cells: application to retina. *Front. Mol. Neurosci.* 8:81. https://doi.org/10.3389/fnmol.2015.00081

Sakmann, B., and E. Neher. 1984. Patch clamp techniques for studying ionic channels in excitable membranes. *Annu. Rev. Physiol.* 46:455–472. https://doi.org/10.1146/annurev.ph.46.030184.002323

Sarao, R., S.K. Gupta, V.J. Auld, and R.J. Dunn. 1991. Developmentally regulated alternative RNA splicing of rat brain sodium channel mRNAs. *Nucleic Acids Res.* 19:5673–5679. https://doi.org/10.1093/nar/19.20.5673

Schrödinger, L. 2015. The PyMol molecular graphics system, version 1.4

Schroeter, A., S. Walzik, S. Blechschmidt, V. Haufe, K. Benndorf, and T. Zimmer. 2010. Structure and function of splice variants of the cardiac voltage-gated sodium channel Na$_v$1.5. *J. Mol. Cell. Cardiol.* 49:16–24. https://doi.org/10.1016/j.yjmcc.2010.04.004

Talvenheimo, J.A., M.M. Tamkun, and W.A. Catterall. 1982. Reconstitution of neurotoxin-stimulated sodium transport by the voltage-sensitive sodium channel purified from rat brain. *J. Biol. Chem.* 257:11868–11871.

Thompson, C.H., R. Ben-Shalom, K.J. Bender, and A.L. George. 2020. Alternative splicing potentiates dysfunction of early-onset epileptic encephalopathy SCN2A variants. *J. Gen. Physiol.* 152:e201912442. https://doi.org/10.1085/jgp.201912442

Tyzio, R., A. Ivanov, C. Bernard, G.L. Holmes, Y. Ben-Ari, and R. Khazipov. 2003. Membrane potential of CA3 hippocampal pyramidal cells during postnatal development. *J. Neurophysiol.* 90:2964–2972. https://doi.org/10.1152/jn.00172.2003

Varga, Z., W. Zhu, A.R. Schubert, J.L. Pardieck, A. Krumholz, E.J. Hsu, M.A. Zaydman, J. Cui, and J.R. Silva. 2015. Direct measurement of cardiac Na+ channel conformations reveals molecular pathologies of inherited mutations. *Circ. Arrhythm. Electrophysiol.* 8:1228–1239. https://doi.org/10.1161/CIRCEP.115.003155

Wahbi, K., V. Algalarrondo, H.M. Becane, V. Fressart, C. Beldjord, K. Azibi, A. Lazarus, N. Berber, H. Radvanyi-Hoffman, T. Stojkovic, et al. 2013. Brugada syndrome and abnormal splicing of SCN5A in myotonic dystrophy type 1. *Arch. Cardiovasc. Dis.* 106:635–643. https://doi.org/10.1016/j.acvd.2013.08.003

Wang, L.J., and E.A. Sobie. 2008. Mathematical model of the neonatal mouse ventricular action potential. *Am. J. Physiol. Heart Circ. Physiol.* 294: H2565–H2575. https://doi.org/10.1152/ajpheart.01376.2007

Yarov-Yarovoy, V., P.G. DeCaen, R.E. Westenbroek, C.Y. Pan, T. Scheuer, D. Baker, and W.A. Catterall. 2012. Structural basis for gating charge movement in the voltage sensor of a sodium channel. *Proc. Natl. Acad. Sci. USA.* 109:E93–E102. https://doi.org/10.1073/pnas.1118434109

Yarowsky, P.J., B.K. Krueger, C.E. Olson, E.C. Clevinger, and R.D. Koos. 1991. Brain and heart sodium channel subtype mRNA expression in rat cerebral cortex. *Proc. Natl. Acad. Sci. USA.* 88:9453–9457. https://doi.org/10.1073/pnas.88.21.9453